

# Time-Varying Multi-Seasonal AR Models

Ganna Fagerberg<sup>a\*</sup>, Mattias Villani<sup>a</sup> and Robert Kohn<sup>b,c</sup>

We propose a seasonal AR model with time-varying parameter processes in both the regular and seasonal parameters. The model is parameterized to guarantee stability at every time point and can accommodate multiple seasonal periods. The time evolution is modeled by dynamic shrinkage processes to allow for long periods of essentially constant parameters, periods of rapid change, and abrupt jumps. A Gibbs sampler is developed with a particle Gibbs update step for the AR parameter trajectories. We show that the near-degeneracy of the model, caused by the dynamic shrinkage processes, makes it challenging to estimate the model by particle methods. To address this, a more robust, faster and accurate approximate sampler based on the extended Kalman filter is proposed. The model and the numerical effectiveness of the Gibbs sampler are investigated on simulated data. An application to more than a century of monthly US industrial production data shows interesting clear changes in seasonality over time, particularly during the Great Depression and the recent Covid-19 pandemic.

*Keywords:* Bayesian inference; Extended Kalman filter; Particle MCMC; Seasonality.

---

<sup>\*</sup>Corresponding author: ganna.fagerberg@stat.su.se. <sup>a</sup>Department of Statistics, Stockholm University.

<sup>b</sup>School of Business, University of New South Wales. <sup>c</sup>Data Analytics Center for Resources and Environments (DARE).

# 1 Introduction

Autoregressive integrated moving average (ARIMA) models, originally popularized in the seminal book by Box and Jenkins (1970), form a parsimonious and versatile class of time series models. ARIMA models have proven invaluable for analyzing time series data, particularly the subclass of AR models. The parsimony of ARIMA models is even more apparent when modeling seasonality with an elegant multiplicative structure that directly extends to multiple seasonal periods, an increasingly common feature in time series data.

A drawback of the Box-Jenkins methodology is the requirement of stationarity, i.e. that the process exhibits constant statistical properties over time, or can be differenced to stationarity. Time series data are often recorded over long study periods, and/or at high-frequency in rapidly changing environments. The statistical characteristics of such time series are likely to undergo substantial changes, which may occur both gradually and suddenly. Differencing the series to achieve stationarity can lead to over-differencing, resulting in misleading inferences (Granger and Joyeux, 1980) and poor forecasts (Makridakis and Hibon, 1997; Smith and Yadav, 1994). Using data only from the most recent regime is wasteful since many correlations are expected to survive regime shifts, and prevents the model from assigning any probability to future regime changes.

A more flexible approach assumes local stationarity where the process is stationary over shorter time segments, or stationary in a small neighborhood around each time point, see e.g. Dahlhaus (2000) for a theoretical framework. One strand of literature explicitly models a small set of stationary regimes, with abrupt jumps between regimes, see e.g. the Markov switching type of models in Hamilton (1989) or change-point models in Chib (1998) and Rosen et al. (2012), and dynamic mixture models in Gerlach et al. (2000). The parameters in time-varying autoregressive (TVAR) models (Prado and West, 2010; Yang et al., 2014; Wood et al., 2011) instead evolve more gradually over time following a stochastic process, typically a random walk with Gaussian innovations. More recently, there has been progress in more realistic models for the parameter evolution that use local-global shrinkage priors

(Polson and Scott, 2010) to cater for smooth gradual changes, periods with no change, as well as abrupt jumps, see e.g. Kalli and Griffin (2014), Kowal et al. (2019), Cadonna et al. (2020) and Knaus and Frühwirth-Schnatter (2023).

Stability restrictions on the AR coefficients are rarely imposed in time-varying parameter AR models; Everitt et al. (2013), Godsill et al. (2004) and Yang et al. (2014) are exceptions with models for time-varying partial autocorrelations. A process with time-varying parameters may however easily drift into the non-stable regions for certain time periods leading to unwanted explosive forecast paths. The main reason for not imposing stability in time-varying models is most likely computational: the stability restrictions are recursive and non-linear, so the Kalman filter or the forward-filtering backward sampling (FFBS) algorithm (Carter and Kohn, 1994; Frühwirth-Schnatter, 1994) can therefore no longer be used for inference.

Seasonality is a neglected aspect of time-varying models, and all of the aforementioned articles deseasonalize the data before the analysis. The regularities provided by seasonality are perhaps the most predictable pattern in a time series and there is much to gain from modeling time-varying seasonality jointly with other model parameters. The absence of time-varying seasonality within the ARIMA framework is probably due to the non-linearity resulting from the multiplicative seasonal structure, again precluding the use of the Kalman filter for inference. This is unfortunate, since the multiplicative seasonal AR representation in Box et al. (2015) directly extends to multiple seasonal patterns, which are an increasingly common feature in many datasets; for example, hourly measurements can exhibit daily, weekly and annual cycles (Xie and Ding, 2020; De Livera et al., 2011).

Our article makes the following contributions. First, a time-varying seasonal AR process is developed where both the regular and the seasonal AR parameters follow the dynamic shrinkage process priors in Kowal et al. (2019). The proposed model is shown to effectively track evolving patterns in parameter values over time, including jumps, while accurately identifying periods of constant parameters. Second, the model is extended to allow for

multiple seasonal periods. Third, we explicitly restrict the parameters to a stable process at every time point using the parameterization in Barndorff-Nielsen and Schou (1973) and Monahan (1984), ensuring that the process is locally stable. Finally, Gibbs sampling algorithms are developed to handle the nonlinearities in the time-varying parameters stemming from both the multiplicative seasonality and stability restrictions.

We propose a fully Bayesian approach and develop a Gibbs sampling algorithm to deal with the non-linearity in the multiplicative seasonal structure and the stability restriction. The algorithm updates the regular and seasonal AR parameters using the particle Gibbs with ancestor sampling (PGAS, Lindsten et al. (2014)) algorithm. PGAS is relatively time-consuming however, and may suffer from degeneracy due to the dynamic shrinkage prior, which encourages parameter paths to remain essentially constant over extended time periods. Therefore, we develop an alternative updating step using the forward-filtering backward sampling (FFBS) algorithm (Carter and Kohn, 1994; Frühwirth-Schnatter, 1994), with the filtering step performed by the extended Kalman filter (Thrun et al., 2005) to handle the two types of non-linearities in the model. The extended Kalman filter is an approximate filter, but we demonstrate that it is quite accurate in seasonal AR models with stability restrictions.

We explore the properties of the proposed model and posterior sampling algorithms in several simulation experiments, and show that the model compares favorably to several widely used time-varying parameter models. Finally, the model is applied to more than a century of monthly industrial production data in the US. We find that the strong seasonality is essentially wiped out during the Great Depression, and is also markedly different during the Covid-19 pandemic.

The proofs and additional results are available in the supplementary material to this article, referenced below with the prefix S, e.g. Figure S1 in Section S1.

## 2 Time-varying multi-seasonal AR processes

Section 2.1 introduces the time-invariant, or static, multi-seasonal AR model (SAR) with stability constraints. The model is then extended in Section 2.2 to have time-varying parameters, using the dynamic shrinkage process (DSP) of Kowal et al. (2019) to regularize the parameter evolution. Finally, Section 2.3 recasts the full model as a nonlinear regression, providing a convenient structure for efficient inference.

### 2.1 Multi-seasonal AR processes with stability restrictions

A general static AR model with one or more seasonal components can be written as (Wei, 2019)

$$\phi(L) \prod_{j=1}^M \Phi_j(L^{s_j})(y_t - m) = \varepsilon_t, \quad (2.1)$$

where  $m$  is the mean,  $L$  is the lag operator with the property  $L^k y_t = y_{t-k}$  and  $\varepsilon_t \stackrel{\text{iid}}{\sim} N(0, \sigma^2)$  is a white noise sequence. The regular AR polynomial of order  $p$  is  $\phi(L) = 1 - \phi_1 L^1 - \phi_2 L^2 - \dots - \phi_p L^p$ . The  $j$ -th seasonal AR component with seasonal period  $s_j$  and seasonal order  $P_j$ , the  $j$ th seasonal component is  $\Phi_j(L^{s_j}) = 1 - \Phi_{j1} L^{s_j} - \Phi_{j2} L^{2s_j} - \dots - \Phi_{jP_j}$ , a polynomial in  $L^{s_j}$ . Here  $M$  stands for the total number of seasonal components.

We denote this model by  $\text{SAR}(p, \mathbf{P})_s$ , where  $p$  is the order of the regular AR polynomial,  $\mathbf{s} = (s_1, \dots, s_M)$  is the vector of seasonal periods, and  $\mathbf{P} = (P_1, \dots, P_M)$  is the corresponding vector of seasonal orders.

When  $M = 1$ , the model in (2.1) reduces to the standard single-seasonal AR model with one regular and one seasonal polynomial with season  $s$ ,  $\text{SAR}(p, P)_s$ :

$$\phi(L) \Phi(L^s)(y_t - m) = \varepsilon_t. \quad (2.2)$$

Models with  $M > 1$  allow for multiple seasonal periods. For example, a SAR model for hourly data with  $M = 2$  and  $\mathbf{s} = (24, 168)$  captures both daily ( $s_1 = 24$ ) and monthly

$(s_2 = 24 \cdot 7 = 168)$  seasonal cycles.

The  $\text{SAR}(p, \mathbf{P})_s$  process in (2.1) is stable if all lag polynomials  $\phi(L)$  and  $\Phi_j(L^{s_j})$  have all their zeros outside the unit circle, i.e.,  $|\phi(z)| \neq 0$  and  $|\Phi_j(z)| \neq 0$ , for  $|z| \leq 1$ . A stable process has many desirable properties, e.g. non-explosive forecast paths, existence of a spectral density, and well-behaved impulse response functions. A stable AR process is also stationary. The model in (2.1) can be extended to include polynomials that apply regular differencing  $\phi(L) = 1 - L$  or seasonal differencing  $\Phi_j(L_j^s) = 1 - L^{s_j}$ . Since the stability restrictions imply the same set of restrictions on the regular and seasonal AR parameters in each polynomial, we now restrict attention to the regular AR polynomial  $\phi(L) = 1 - \phi_1 L - \dots - \phi_p L^p$ .

To enforce stability we use the reparametrisation in Barndorff-Nielsen and Schou (1973) and Monahan (1984) to map a set of unconstrained real-valued coefficients to the set of stable parameters, i.e. parameters that determine a stable process. Let  $\mathbb{S}^p \subset \mathbb{R}^p$  denote the region in parameter space where the  $\text{AR}(p)$  process is stable. The reparameterization is defined as follows.

**Definition 1** (stability parameterization). *An  $\text{AR}(p)$  process can be restricted to be stable by a 1:1 and onto map*

$$\boldsymbol{\theta} \rightarrow \mathbf{r} \rightarrow \boldsymbol{\phi}.$$

of unrestricted parameters  $\boldsymbol{\theta} = (\theta_1, \dots, \theta_p)^\top \in \mathbb{R}^p$  via the partial autocorrelations  $\mathbf{r} = (r_1, \dots, r_p)^\top \in (-1, 1)^p$  to the stable AR parameters  $\boldsymbol{\phi} = (\phi_1, \dots, \phi_p)^\top \in \mathbb{S}^p$ . The mapping from  $\mathbf{r}$  to  $\boldsymbol{\phi}$  is given by setting  $\phi_{1,1} = r_1$  followed by the recursion

$$\phi_{k,j} = \phi_{k-1,j} - r_k \phi_{k-1,k-j}, \quad \text{for } k = 2, \dots, p \text{ and } j = 1, \dots, k-1,$$

and finally returning  $\boldsymbol{\phi} = (\phi_{p,1}, \dots, \phi_{p,p})^\top$ , where  $\phi_{p,p} = r_p$ .

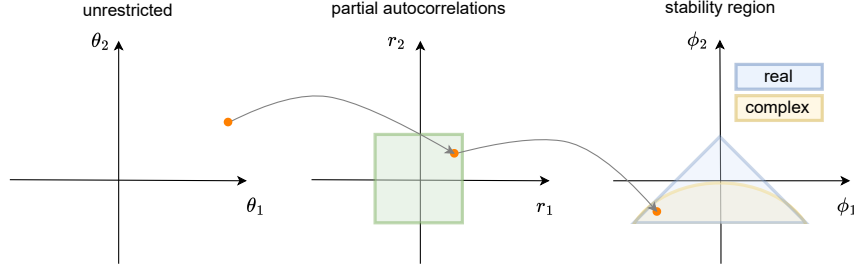


Figure 1: Illustrating the stability parametrization from an AR(2) process from the unrestricted  $\boldsymbol{\theta} = (\theta_1, \theta_2)^\top \in \mathbb{R}^2$  (left) via the partial autocorrelations  $\mathbf{r} = (r_1, r_2)^\top \in (-1, 1)^2$  (middle) to the AR parameters  $\boldsymbol{\phi} = (\phi_1, \phi_2)^\top$  (right); the regions with real (blue) and complex (beige) roots are also shown.

We use the  $\boldsymbol{\theta} \rightarrow \mathbf{r}$  transformation suggested by Monahan (1984)

$$r_k = \frac{\theta_k}{\sqrt{1 + \theta_k^2}} \quad \text{for } k = 1, \dots, p. \quad (2.3)$$

Figure 1 illustrates the two mappings involved in the parametrization.

The unrestricted parameters  $\boldsymbol{\theta} = (\theta_1, \dots, \theta_p)^\top$  in (2.3) are merely technical devices and are not interpretable. The following lemma gives the prior on  $\boldsymbol{\theta}$  which implies a uniform distribution over the stable/stationary region for the AR parameters; its proof is in Section S1.1. A uniform distribution can be used as a baseline for more informative distributions.

**Lemma 1.** *Let  $\boldsymbol{\phi} = \mathbf{g}(\boldsymbol{\theta})$  be the mapping in Definition 1, and let  $\theta_1, \dots, \theta_p$  be independently distributed as*

$$\theta_k \sim \begin{cases} t(k+1, 0, \frac{1}{\sqrt{k+1}}) & \text{if } k \text{ is odd} \\ t_{\text{skew}}\left(\frac{k}{2}, \frac{k+2}{2}, 0, \frac{1}{\sqrt{k+1}}\right) & \text{if } k \text{ is even;} \end{cases} \quad (2.4)$$

then  $\boldsymbol{\phi} = \mathbf{g}(\boldsymbol{\theta})$  is uniform over the stability region in  $\boldsymbol{\phi}$ -space. Here  $t(v, \mu, \sigma)$  is the usual  $t$ -distribution with  $v$  degrees of freedom translated by  $\mu$  and scaled by  $\sigma$ , and  $t_{\text{skew}}(a, b, \mu, \sigma)$  is the skew- $t$  extension in Jones and Faddy (2003).

## 2.2 Locally stable time-varying multi-seasonal AR processes

The time-varying, or dynamic, AR model with multiple seasonal components

$$\phi_t(L) \prod_{j=1}^M \Phi_{jt}(L^{s_j}) y_t = \varepsilon_t, \quad N(0, \sigma^2) \quad (2.5)$$

extends the model in (2.1) with time-varying regular and seasonal AR polynomials  $\phi_t(L) = 1 - \phi_{1t}L^1 - \phi_{2t}L^2 - \dots - \phi_{pt}L^p$  and  $\Phi_{jt}(L^{s_j}) = 1 - \Phi_{j1t}L^{s_j} - \Phi_{j2t}L^{2s_j} - \dots - \Phi_{jp_jt}L^{P_js_j}$ , respectively.

The errors  $\varepsilon_t$  can be generalized to have time-varying noise variance; see Section S3.6 and the empirical application in Section 5. We also assume that the process has a zero mean, but a non-zero time-varying mean  $m_t$  can be included in the model. We denote this model by  $\text{TVSAR}(p, \mathbf{P})_{\mathbf{s}}$ , where, as before,  $\mathbf{s} = (s_1, \dots, s_M)$  is a vector with the  $M$  seasonal periods and  $\mathbf{P} = (P_1, \dots, P_M)$  are the corresponding seasonal lag orders.

To enforce local stability in the dynamic AR process, we employ the parameterization described in Definition 1 to each regular and seasonal AR polynomial in (2.5). As in the static case, we restrict our attention to the regular AR polynomial, noting that the same mapping applies to the seasonal polynomials as well.

At each time period  $t$ , we map the unrestricted time-varying parameters  $\boldsymbol{\theta}_t = (\theta_{1t}, \dots, \theta_{pt})^\top$  to the time-varying AR parameters  $\boldsymbol{\phi}_t = (\phi_{1t}, \dots, \phi_{pt})^\top$ . The unrestricted parameters  $\boldsymbol{\theta}_t$  evolve over time following the dynamic shrinkage process (DSP) prior in Kowal et al. (2019). The DSP is a time series extension of the widely used horseshoe prior (Carvalho et al., 2010), allowing the parameters to be essentially unchanged for long periods followed by large jumps or potentially persistent periods of rapid change. The process for the evolving TVSAR

parameters in any given AR polynomial with  $p$  lags is

$$\begin{aligned}\boldsymbol{\phi}_t &= \mathbf{g}(\boldsymbol{\theta}_t) \\ \theta_{kt} &= \theta_{k,t-1} + \nu_{kt}, & \nu_{kt} &\stackrel{\text{indep}}{\sim} N(0, \exp(h_{kt})) \\ h_{kt} &= \mu_k + \kappa_k(h_{k,t-1} - \mu_k) + \eta_{kt}, & \eta_{kt} &\stackrel{\text{iid}}{\sim} Z(1/2, 1/2, 0, 1),\end{aligned}\tag{2.6}$$

for  $k = 1, \dots, p$ , where  $\boldsymbol{\phi}_t = \mathbf{g}(\boldsymbol{\theta}_t)$  maps the unrestricted parameters  $\boldsymbol{\theta}_t \in \mathbb{R}^p$  to the stable parameters  $\boldsymbol{\phi}_t \in \mathbb{S}^p$ . The global means,  $\boldsymbol{\mu} = (\mu_1, \dots, \mu_p)^\top$ , of log-volatilities,  $\boldsymbol{h}_t = (h_{1t}, \dots, h_{pt})^\top$ , control the overall degree of time-variation in  $\boldsymbol{\theta}_t$  and consequently in  $\boldsymbol{\phi}_t$ . The parameter  $\kappa_k$  regulates the persistence of the log-volatility process  $h_{kt}$  for the  $k$ th parameter. The innovations to the log-volatility are drawn from the heavy-tailed  $Z$ -distribution (Barndorff-Nielsen et al., 1982) with zero location and unit scale parameters. It is straightforward to add a scale parameter  $\sigma_\eta$  to  $\eta_{kt} \sim Z(1/2, 1/2, 0, \sigma_\eta)$ , but it is unnecessary in our model. These innovations admit a scale-mixture representation with Pólya-Gamma distributed mixing variables, yielding a conditionally Gaussian model amenable to efficient inference via data augmentation (Kowal et al., 2019).

A small global  $\mu_k$  gives a prior with long periods of essentially constant evolution in  $\theta_k$ . When a positive local heavy-tailed  $\eta_{kt}$  innovation occurs, it causes the log-volatility to temporarily spike and remain high for a duration governed by the persistence parameter  $\kappa_k$ . To see the connection to the original horseshoe prior in Carvalho et al. (2010), consider the case with no persistence,  $\kappa_k = 0$ . The variance of the innovations to the  $k$ th parameter is then  $\exp(h_{kt}) = \tau_k^2 \lambda_{kt}^2$ , where  $\tau_k^2 = \exp(\mu_k)$  is the global variance and  $\lambda_{kt}^2 = \exp(\eta_{kt})$  is the time-varying local variance. The implied prior on each  $\lambda_{kt}$  is  $C^+(0, 1)$ , i.e. a heavy tailed half-Cauchy as in the original horseshoe prior. Kowal et al. (2019) demonstrate that the DSP prior with  $0 < \kappa < 1$  gives additional shrinkage in a time period that follows a period of heavy shrinkage. For a comprehensive treatment of the DSP process, see Kowal et al. (2019).

Lemma 1 gives the prior that implies a uniform distribution over the stability region. The log-volatilities at time  $t = 0$  are  $\mathbf{h}_0 = \boldsymbol{\mu} + \boldsymbol{\eta}_0$  with the elements of  $\boldsymbol{\eta}_0$  independent  $Z \sim (1/2, 1/2, 0, 1)$  a priori. The prior for each  $\kappa_k \sim \text{TN}(\kappa_0, \psi_0^2, -1, 1)$  is a normal truncated to  $(-1, 1)$ , giving an easily sampled truncated normal as conditional posterior. Kowal et al. (2019) use a Pólya-Gamma construction for the prior on the global means  $\mu_k$  to obtain the original  $C^+(0, 1)$  horseshoe prior for  $\tau_k = \exp(\mu_k/2)$ . This choice for the horseshoe prior is questioned by Piironen and Vehtari (2017) and we use  $\mu_k \sim N(\mu_0, \sigma_0^2)$ , implying a log normal prior for  $\tau_k$ .

The DSP prior governs the time-variation in the unrestricted parameters  $\boldsymbol{\theta}_t$ . The nonlinear mapping from the  $\boldsymbol{\theta}_t$  to the AR coefficients  $\boldsymbol{\phi}_t$  is smooth and invertible, and preserves the qualitative properties of the DSP prior, i.e. the ability to generate long spells of essentially constant parameter, rapid changes and jumps; see Section S2.

### 2.3 The multi-seasonal TV-AR model as a nonlinear regression

The multi-seasonal TVSAR( $p, \mathbf{P}$ )<sub>s</sub> model in (2.5) can be written as a single AR polynomial model by multiplying out the regular and  $M$  seasonal AR polynomials  $\phi_t(L) \prod_{j=1}^M \Phi_{jt}(L^{s_j}) = \tilde{\phi}_t(L)$  and moving all lags to the right-hand side to obtain the regression model

$$y_t = \mathbf{x}_t^\top \tilde{\boldsymbol{\phi}}_t + \varepsilon_t, \quad \varepsilon_t \stackrel{\text{iid}}{\sim} N(0, \sigma^2), \quad (2.7)$$

where  $\mathbf{x}_t$  is a vector containing all lags  $y_{t-k}$  for which the coefficients in  $\tilde{\phi}_t(L)$  are non-zero and the vector  $\tilde{\boldsymbol{\phi}}_t$  collects the coefficients for those lags. The elements of  $\tilde{\boldsymbol{\phi}}_t$  are products of the AR parameters in the different polynomials. For example, consider a model with a regular component with one lag and one seasonal component with period  $s$  and one lag

$$(1 - \phi_{1t}L)(1 - \Phi_{1t}L^s)y_t = \varepsilon_t. \quad (2.8)$$

Multiplying out the two polynomials on the left hand side of (2.8) and rearranging, the model can be written

$$y_t = \phi_{1t} y_{t-1} + \Phi_{1t} y_{t-s} - \phi_{1t} \Phi_{1t} y_{t-(1+s)} + \varepsilon_t, \quad (2.9)$$

so  $\mathbf{x}_t = (y_{t-1}, y_{t-s}, y_{t-(1+s)})^\top$  and  $\tilde{\boldsymbol{\phi}}_t = (\phi_{1t}, \Phi_{1t}, \phi_{1t} \Phi_{1t})^\top$  in (2.7). The three-dimensional vector of regression coefficients  $\tilde{\boldsymbol{\phi}}_t$  is a nonlinear transformation of the two unrestricted AR parameters at time  $t$ . A general TVSAR model with one regular and  $M$  seasonal polynomials involves a nonlinear transformation with a total of  $r = p + \sum_{j=1}^M P_j$  unrestricted time-varying AR parameters.

We use the conditional likelihood function of the seasonal AR model based on the regression formulation in (2.7), conditional on  $p_{\max}$  pre-sample values  $y_0, y_{-1}, \dots, y_{-p_{\max}+1}$  where  $p_{\max}$  is the maximal lag order in  $\mathbf{x}_t$ . An alternative approach is to use the exact likelihood (Hamilton, 1994) to avoid the loss of initial data, or to infer the initial observations as a separate step in the algorithm.

In summary, the seasonal AR model with dynamic shrinkage priors is

$$\begin{aligned} y_t &= \mathbf{x}_t^\top \tilde{\mathbf{g}}(\boldsymbol{\theta}_t) + \varepsilon_t, & \varepsilon_t &\stackrel{\text{iid}}{\sim} N(0, \sigma^2) \\ \boldsymbol{\theta}_t &= \boldsymbol{\theta}_{t-1} + \boldsymbol{\nu}_t, & \boldsymbol{\nu}_t &\stackrel{\text{indep}}{\sim} N(\mathbf{0}, \text{Diag}(\exp(\mathbf{h}_t))) \\ \mathbf{h}_t &= \boldsymbol{\mu} + \boldsymbol{\kappa}(\mathbf{h}_{t-1} - \boldsymbol{\mu}) + \boldsymbol{\eta}_t, & \eta_{kt} &\stackrel{\text{iid}}{\sim} Z(1/2, 1/2, 0, 1), \end{aligned} \quad (2.10)$$

where  $\boldsymbol{\theta}_t$  is a vector with all  $r = (p + \sum_{j=1}^M P_j)$  AR coefficients and  $\tilde{\boldsymbol{\phi}}_t = \tilde{\mathbf{g}}(\boldsymbol{\theta}_t)$  maps the coefficients in each AR polynomial to the stability region followed by polynomial multiplication leading to  $\tilde{\boldsymbol{\phi}}_t$  in (2.7). The  $r \times r$  matrix  $\boldsymbol{\kappa}$  is diagonal with  $(\kappa_1, \dots, \kappa_r)^\top$  on its main diagonal and  $\text{Diag}(\exp(\mathbf{h}_t))$  is a diagonal matrix having  $\exp(\mathbf{h}_t) = (\exp(h_{1t}), \dots, \exp(h_{rt}))^\top$  on its main diagonal.

### 3 Bayesian inference for time-varying multi-seasonal AR

The joint posterior distribution  $p(\boldsymbol{\theta}_{0:T}, \mathbf{h}_{0:T}, \sigma_{1:T}, \boldsymbol{\mu}, \boldsymbol{\kappa} | y_{1:T})$  is sampled using a block Gibbs sampler, with each of the above parameter vectors as separate updating blocks; here the notation  $\boldsymbol{\theta}_{0:T}$  means the sequence of all  $r$  unrestricted AR parameters  $\boldsymbol{\theta}_t$  for  $t = 0, 1, \dots, T$ . See Algorithm S1 in the supplementary material for an overview.

We now explain the updating step for  $\boldsymbol{\theta}_{0:T}$ , leaving the details of the updating steps for  $\boldsymbol{\mu}$ ,  $\boldsymbol{\kappa}$  and  $\mathbf{h}_{0:T}$  to Section S3.

#### 3.1 Updating the parameter paths

Conditional on all other parameters, the TVSAR model in (2.10) can be expressed as the following state-space model with  $\boldsymbol{\theta}_t$  as the state vector

$$\boldsymbol{\theta}_0 \sim \text{Uniform}(\mathbb{S}) \quad (3.1)$$

$$\boldsymbol{\theta}_t | \boldsymbol{\theta}_{t-1} \sim N(\boldsymbol{\theta}_{t-1}, \text{Diag}(\exp(\mathbf{h}_t))) \quad (3.2)$$

$$y_t | \boldsymbol{\theta}_t \sim N(\mathbf{x}_t^\top \tilde{\mathbf{g}}(\boldsymbol{\theta}_t), \sigma^2), \quad (3.3)$$

where  $\text{Uniform}(\mathbb{S})$  denotes the uniform distribution over the stability region for the implied  $\boldsymbol{\phi}_0$  in each AR polynomial. Note that the state transition model in (3.2) is linear and heteroscedastic Gaussian, and the measurement model in (3.3) is nonlinear with Gaussian additive errors.

Our goal is to design a Gibbs updating step where that draws from the joint conditional posterior of the parameter paths  $p(\boldsymbol{\theta}_{0:T} | y_{1:T}, \cdot)$ , using the dot  $\cdot$  as a placeholder for all the other parameters in the model. Sampling is ideally performed by the following two steps:

1. compute the sequence of *filtering distributions*  $p(\boldsymbol{\theta}_t | y_{1:t}, \cdot)$  for  $t = 0, \dots, T$ ;
2. sample from the *joint smoothing distribution*  $p(\boldsymbol{\theta}_{0:T} | y_{1:T}, \cdot)$  via backward sampling, starting from the final filtering distribution  $p(\boldsymbol{\theta}_T | y_{1:T}, \cdot)$  and iterate back in time.

For linear Gaussian models, the filtering posteriors are Gaussian and can be computed recursively in closed form by the Kalman filter recursions. The backward sampling step then simulates from multivariate Gaussian distributions. This is the Forward Filtering and Backward Sampling (FFBS) algorithm developed by Carter and Kohn (1994) and Frühwirth-Schnatter (1994).

Conditional on the log-volatilities  $\mathbf{h}_{0:T}$ , the model in (3.1)-(3.3) is linear Gaussian in the transition model, but non-linear Gaussian in the measurement equation. We use the Particle Gibbs with Ancestor Sampling (PGAS) algorithm in Lindsten et al. (2014) to sample from the conditional posterior of parameter trajectory  $\boldsymbol{\theta}_{0:T}$ . Section S4 in the Supplementary material explains the PGAS updating step, and refer to Lindsten et al. (2014) for further details. The PGAS algorithm can suffer from particle degeneracy in near-degenerate models (Lindsten et al., 2015), for example when the innovations in the transition model have close to zero variance for some  $t$ . This often occurs with the TVSAR in (2.10) since the dynamic shrinkage priors encourage parameters to remain constant for extended time periods.

For near-degenerate TVSAR models we suggest an alternative updating step for  $\boldsymbol{\theta}_{0:T}$  based on an approximate sampling step that replaces the Kalman filter in the FFBS sampler with the extended Kalman filter (EKF). The EKF linearizes the nonlinear observation and/or state equations via first-order Taylor expansions around the prior propagated state at each time step; see Thrun et al. (2005) for an introduction to the EKF. The derivatives needed in the EKF are computed by automatic differentiation (Baydin et al., 2018), making it possible to write fast and general code for TVSAR with any number of seasonal periods. The algorithm uses the same backward simulation recursions as in the FFBS algorithm; we call this algorithm FFBSx, where x is a mnemonic for extended. The extended Kalman filter needs a Gaussian prior for the initial state. We therefore approximate the prior in Lemma 1 when using FFBSx by the closest normal distribution with respect to the Hellinger metric; see Section S1.2 for details.

The accuracy of the EKF algorithm depends on the degree of nonlinearity in the measurement

and transition equations, and how much the state and measurement noise deviate from Gaussian distributions. The TVSAR is well suited for the EKF since the state transition remains linear and Gaussian and the non-linearity is only present in the observation equation, which still has additive Gaussian errors. Our empirical results in Sections 4 and 5 show that the algorithm is fast, robust and accurate for the TVSAR.

## 4 Simulation experiments

We conduct several simulation experiments to evaluate the effectiveness and robustness of the multi-seasonal AR model, assess the performance of the various simulation algorithms, and compare the TSVAR model against a set of benchmark models. The experimental setups include data generating processes with single and multiple seasonalities, and also an experiment where the estimated model has redundant lags.

### 4.1 Setup and benchmark models

We simulate 100 time series from the data generating process for each experiment. The simulated time series consist of  $T = 1000$  observations, and we generate 10 000 draws from the posterior distribution for each method, after a burn-in of 3000 iterations. The post burn-in draws are thinned by a factor of 10 before computing the spectral densities. In Experiments 1 and 2, we fit the same number of lags as the number of lags in the data generating process. Experiment 3 in Section S5.4 of the supplementary material shows that the dynamic shrinkage prior is able to shrink redundant lags to zero in the TVSAR when a model with too many lags is applied to the data. The empirical application in Section 5 uses the log predictive scores to determine the optimal number of lags.

Our proposed models and algorithms are compared with the following alternatives: a linear time-varying AR model with dynamic shrinkage priors (Kowal et al., 2019) without explicit stability restrictions implemented in the R package `dsp`, a kernel smoothing estimation

method using the `tvReg` package in R (Casas and Fernandez-Casal, 2023) and the time-varying AR with the dynamic triple gamma shrinkage prior (Knaus and Frühwirth-Schnatter, 2023) implemented as the function `shrinkDTVP` in the `shrinkTVP` package (Knaus et al., 2021). We also compare with the `AdaptSpec` method (Rosen et al., 2012; Bertolacci, 2021) that estimates a local spectral density using smoothing splines over time segments learned by the algorithm. We use default settings for all benchmark methods with the exception of `AdaptSpec`, where the default number of spline knots is increased to 40 instead of the default with seven spline knots and the maximum number of segments is increased from the default 10 to 20. Preliminary experiments show that this gives `AdaptSpec` a better chance to capture the highly multimodal spectral density in seasonal models.

All of the time-varying AR benchmark models are designed for non-seasonal data. To give a fairer comparison, we construct seasonally adapted versions of the benchmark models. For example, a  $\text{TVSAR}(1, 1)_{12}$  can be formulated as a regular AR with non-zero coefficient  $\phi_1$  at lag 1,  $\Phi_1$  at lag 12 and  $-\phi_1\Phi_1$  at lag 13, see (2.9). We then fit benchmark models with 13 lags and impose zero-restrictions on the coefficients for lags 2 to 11. Note, however, that the coefficient on lag 13 is estimated as an unrestricted coefficient in the benchmark models since they cannot handle the non-linear multiplicative structure. The time-domain benchmark models do not impose stability/stationarity restrictions, and we therefore discard posterior draws outside the stability region to ensure a well-defined spectral density. Discarding non-stable draws can be formalized as using a prior truncated to the stability region with rejection sampling after the MCMC, where the acceptance probability is zero for unstable draws and one for stable draws; see Appendix B in Cogley and Sargent (2005). This however requires the whole trajectory from  $t = 1$  to  $t = T$  to be accepted/rejected, which leads to too many rejected draws. We instead use a pragmatic approach for the benchmark models by accepting or rejecting individually for different time periods. The difficulty with rejection sampling of whole trajectories shows the advantage of formally imposing stability restrictions in the  $\text{TVSAR}$  model.

In all three experiments, we use iid priors for the static parameters:  $\mu \sim N(-15, 3^2)$ ,  $\kappa \sim TN(0.5, 0.3^2, -1, 1)$  and  $\sigma^2 \sim \text{Inv-}\chi^2(3, s^2)$ , a scaled inverse chi-squared distribution, where  $s^2$  is the residual variance from a linear AR model fitted to the time series. Note that  $\mu$  is on the log-scale, so the implied prior on the global standard deviation  $\tau = \exp(\mu/2)$  is log normal with 95% equal tail interval  $(2.92 \cdot 10^{-5}, 0.01)$ . This prior encourages parameters to remain constant, but, as we will see, still allows for sizeable jumps via the heavy-tailed log-volatility innovations,  $\eta_t$ .

## 4.2 Performance metrics

Since the set of compared models includes models in both the time and frequency domains, and models with both multiplicative and additive structures, we compare the methods based on their ability to estimate the time-varying spectral density. The spectral density of a seasonal AR process at time  $t$  is (Wei, 2019)

$$f(t, \omega) = \frac{\sigma^2}{\pi} \frac{1}{|\phi_{pt}(e^{-i\omega})|^2} \frac{1}{|\Phi_{Pt}(e^{-is\omega})|^2} \text{ for } \omega \in (0, \pi) \text{ and } t = 1, \dots, T, \quad (4.1)$$

where  $\phi_{pt}(L)$  and  $\Phi_{Pt}(L^s)$  are the usual regular and seasonal AR lag polynomials at time  $t$  and  $\omega \in (0, \pi]$  is the radial frequency. This expression extends to seasonal AR models with multiple seasonal periods in the obvious way. Following Rosen et al. (2012), we use the Mean Square Error (MSE) of the estimated log spectral density over all time periods as the performance metric

$$\text{MSE}(\widehat{\log f}) = \frac{1}{Tm} \sum_{t=1}^T \sum_{k=1}^m (\widehat{\log f(t, \omega_k)} - \log f(t, \omega_k))^2, \quad (4.2)$$

where  $\log f(t, \omega)$  is the true log spectral density at time  $t$  and frequency  $\omega$ ;  $\widehat{\log f(t, \omega)}$  is its estimate, and  $m = 314$  is the total number of frequencies on a grid from 0.01 to  $\pi$ . The posterior median of the log spectral density  $\log f(t, \omega)$  is used as the point estimate in the

Bayesian models since it is more robust to outliers in the MCMC.

### 4.3 Experiment 1 - Single-seasonal TVSAR

The first experiment simulates data from the time-varying TVSAR(2, 2)<sub>12</sub>

$$(1 - \phi_{1t}L - \phi_{2t}L^2)(1 - \Phi_{1t}L^{12} - \Phi_{2t}L^{24})y_t = \varepsilon_t, \quad (4.3)$$

where  $\varepsilon_t \sim N(0, 1)$ . The beige lines in Figure 2 show the evolution of the regular AR parameters  $\phi_{kt}$  and the seasonal AR parameters  $\Phi_{kt}$ ; for details, see equations (S5.2) and (S5.3) in Section S5.1 of the supplementary material.

We first explore the numerical performance of the Gibbs sampler with a PGAS update step for different numbers of particles. As explained in Section 3.1, particle Gibbs samplers like PGAS can struggle when the state transition model is nearly degenerate. Our simulation setup is a rather extreme case of near-degeneracy where some parameters are constant over extended segments or even constant throughout time.

We compare PGAS with the more robust FFBSx algorithms based on the extended Kalman filter. The potential approximation errors from FFBSx can be attributed to the two nonlinearities in the TVSAR: one from its the multiplicative structure and another from the stability restrictions. Therefore, we also apply the FFBSx algorithm to a TVSAR model without imposing the stability restrictions. The FFBSx applied to the TVSAR with stability restrictions is referred to as FFBSx-m (where the m stands for the Monahan transformation in (2.3), while FFBSx-l refers to FFBSx applied to the TVSAR model without stability restrictions (l stands for linear)).

Figure 2 assesses the convergence of the algorithms by plotting the posterior medians and equal-tail 95% credible intervals from five different runs on the same dataset, each with different initial values. The initial values for the global parameters are set so that  $\mu_k = \mu$  and  $\kappa_k = \kappa$  for all  $k$ , with  $\mu$  and  $\kappa$  drawn from their respective priors in each run of the

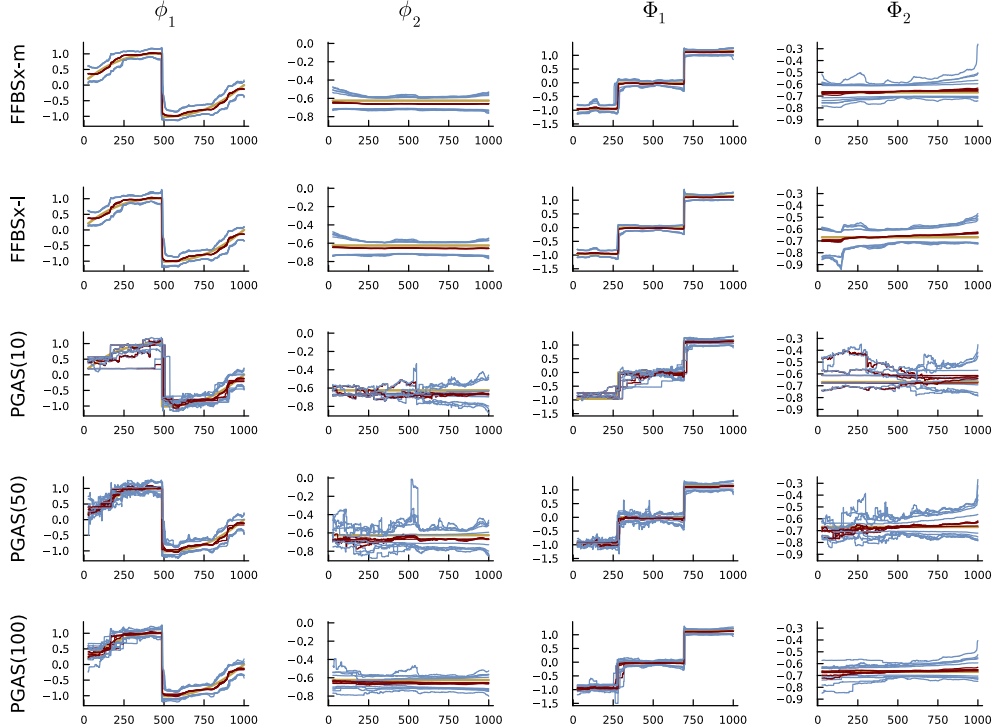


Figure 2: Experiment 1. Assessing MCMC convergence by re-estimating the model on the same dataset with five different initial values. The red and blue lines are posterior medians and 95% equal tail credible bands over time for each of the five repeated runs. The beige line is the true parameter evolution in the  $\phi$ -parameterization.

algorithm. The initial values for the log-volatilities  $h_{k,t}$  are set to the randomly generated  $\mu$  for all  $k$  and  $t$ . PGAS( $N$ ) is the PGAS algorithm with  $N$  particles. All PGAS algorithms use a proposal at time  $t = 0$  from an initial FFBSSx-m run with 500 iterations. The results in Figure 2 use a minimal offset of  $10^{-16}$  (close to the machine precision in Julia) in the update for  $\mathbf{h}_{0:T}$ ; we return to this choice of offset below.

Figure 2 shows that both the FFBSSx and PGAS samplers accurately capture the evolving patterns of varying complexities and correctly identify constant parameters. However, the PGAS sampler struggles with the near-degeneracy in this example, requiring at least 100 particles to achieve relatively stable results across different runs. In contrast, the FFBSSx samplers are stable, while yielding a very similar posterior to PGAS(100). This is reassuring since FFBSSx is an approximate algorithm. Moreover, the additional nonlinearity handled by FFBSSx-m compared to single nonlinearity in FFBSSx-l does not deteriorate stability and fit.

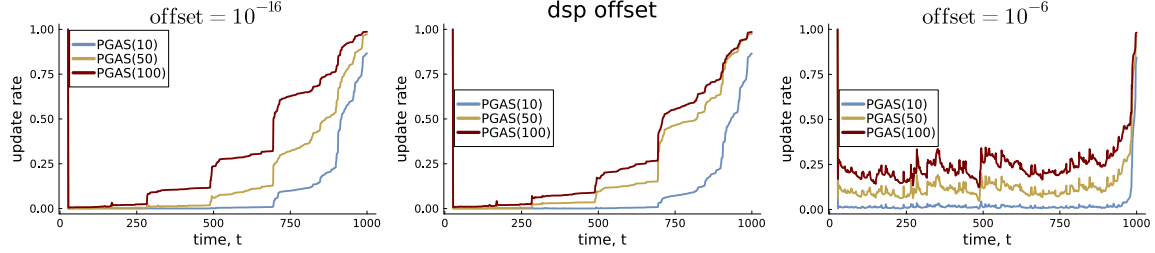


Figure 3: Experiment 1. PGAS update rates for three different offsets in the log-volatility model for  $\mathbf{h}_t$  for different number of particles.

The effective sample size (ESS, (Chopin and Papaspiliopoulos, 2020)) of the PGAS algorithms can be very low for the earlier part of the time period, while the ESS for the FFBsX algorithms are larger and stable across time; see Table S2 in Section S5.1 for the ESS for the spectral density at some selected time periods and frequencies. The relatively low ESS comes from learning the global and local variances in the dynamic shrinkage process, a well known challenging issue with horseshoe-type of priors (Piironen and Vehtari, 2017), an area which would benefit from more research.

The FFBsX samplers are substantially faster than the PGAS samplers. One thousand draws with FFBsX-m takes 25 seconds, compared to 23 seconds for FFBsX-l and 258 seconds with PGAS(100). The timings are for Julia code on a single core of an Apple M1 processor with 16 GB of RAM memory; the code is not optimized and timings should therefore be considered as rather loose upper bounds. The robustness, speed and accuracy of FFBsX makes it our preferred algorithm. When we refer to the TVSAR model below without mentioning the sampling algorithm, we mean the TVSAR with stability restrictions estimated with the FFBsX algorithm.

Figure 3 plots the update rates for the TVSAR parameters for the PGAS algorithms for three different offsets in the update for  $\mathbf{h}_{1:T}$  in (S3.5). Offsets are standard in stochastic volatility models (Kim et al., 1998) to avoid taking logs of zero, but also artificially inflates the inferred  $h_t$ , which can be important when using the DSP prior. The dsp offset in Figure 3 uses the rule in (S3.6) from the `dsp` package (Kowal et al., 2019). The update rate is the proportion of times the parameter changes over the iterations and is here computed on all

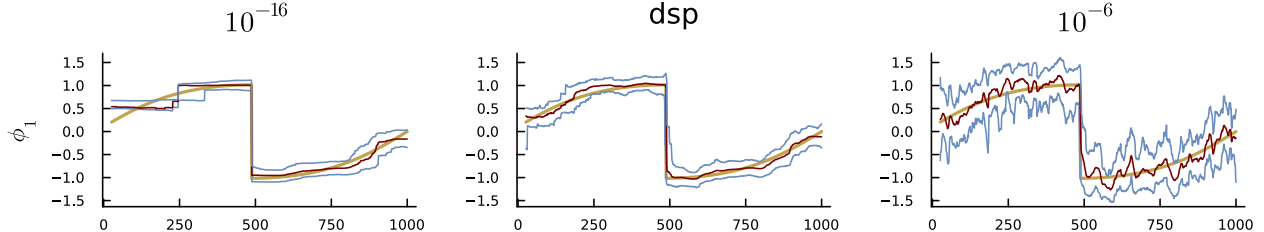


Figure 4: Experiment 1. Posterior median and 95% credible intervals for  $\phi_{1t}$  from PGAS(100) from one run for the three different offsets in the log-volatility model for  $\mathbf{h}_t$ . See Figure S5 of the supplement for the remaining parameters.

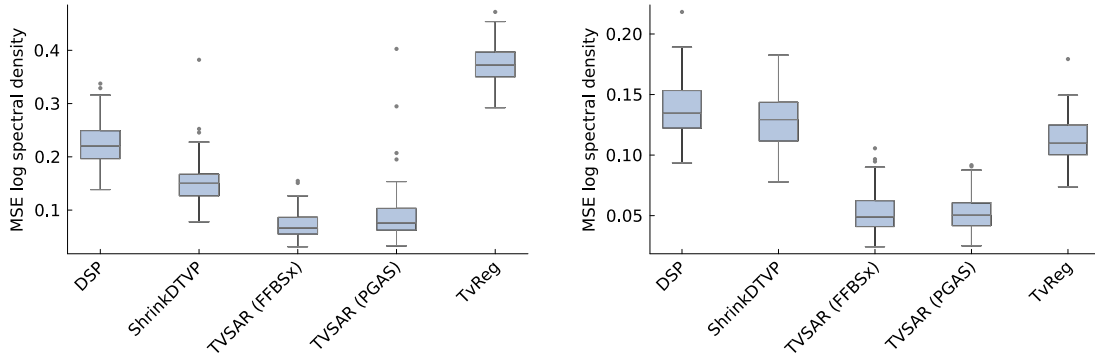


Figure 5: Box plots of the MSE for the log spectral density over time and frequency from 100 simulated datasets for Experiment 1 (left) and Experiment 2 (right).

10 000 draws before thinning. A larger offset makes the state transition less degenerate with higher update rates, but with more wiggly parameter evolutions, making it harder to detect constant parameters; see Figure 4 for  $\phi_{1t}$  and Figure S5 for the remaining parameters. Importantly, the results in Figure 2 are based on the smallest offset  $10^{-16}$ , showing that FFBSx works well even with essentially no offset. The effect of the near-degeneracy on PGAS can be less pronounced in other examples; see Experiment 2 below, and the results for TVSAR with one regular and one seasonal lag in Section S5.2.

The left graph of Figure 5 displays box plots of the MSE metric in (4.2) for the compared models over the 100 simulated datasets. The median MSE for AdaptSpec is approximately 0.9 with a couple of outliers around 1.5, and is not shown in Figure 5 to make the vertical scale more readable for comparing the other methods; AdaptSpec is not specifically designed for seasonal data and therefore struggles here. The TVSAR model estimated with the FFBSx

algorithm performs best among the compared models, with a consistently low MSE across the datasets. The performance of the TVSAR model without stability restrictions is similar and is not shown. The linear DSP model outperforms TvReg with a sizeable margin, but the dynamic triple Gamma shrinkage prior (ShrinkDTVP) is the best among the benchmark methods.

Figure 6 displays heatmaps of the estimated time-varying log spectral density for the different models. Following Rosen et al. (2012), we plot the posterior median of the time varying log spectral densities for three different datasets, corresponding to the 10%, 50%, and 90% percentiles of the MSE values for each method. This show how each method performs when it performs well (10%), average (50%), and poorly (90%). Note that the columns of Figure 6 are therefore for potentially different datasets for the different methods. See Figures S6 and S7 in the supplementary material for an alternative view where the fitted spectral densities are plotted at some selected times and frequencies. Our TVSAR model (with stability restrictions, estimated by FFBsx) gives less wiggly fits than DSP, while TvReg oversmooths. ShrinkDTVP performs relatively well in capturing the jumps, but is also more wiggly than the TVSAR model.

#### 4.4 Experiment 2 - Multi-seasonal TVSAR

The second experiment simulates data from a multi-seasonal TVSAR with two seasonal periods  $\mathbf{s} = (4, 12)$ , non-seasonal order  $p = 1$  and seasonal orders  $\mathbf{P} = (1, 1)$  (i.e., one lag for each seasonal period). This corresponds to the  $\text{TVSAR}(p = 1, \mathbf{P} = [1, 1])_{[4,12]}$  model

$$(1 - \phi_{11t}L)(1 - \Phi_{11t}L^4)(1 - \Phi_{21t}L^{12})y_t = \varepsilon_t, \quad (4.4)$$

with  $\varepsilon_t \sim N(0, 1)$ . The time evolution of the parameters are plotted as beige lines in Figure 7; see (S5.7) and in Section S5.3 of the supplementary material for details.

Figure 7 shows that the five runs of FFBsx-m are nearly identical and very close to the

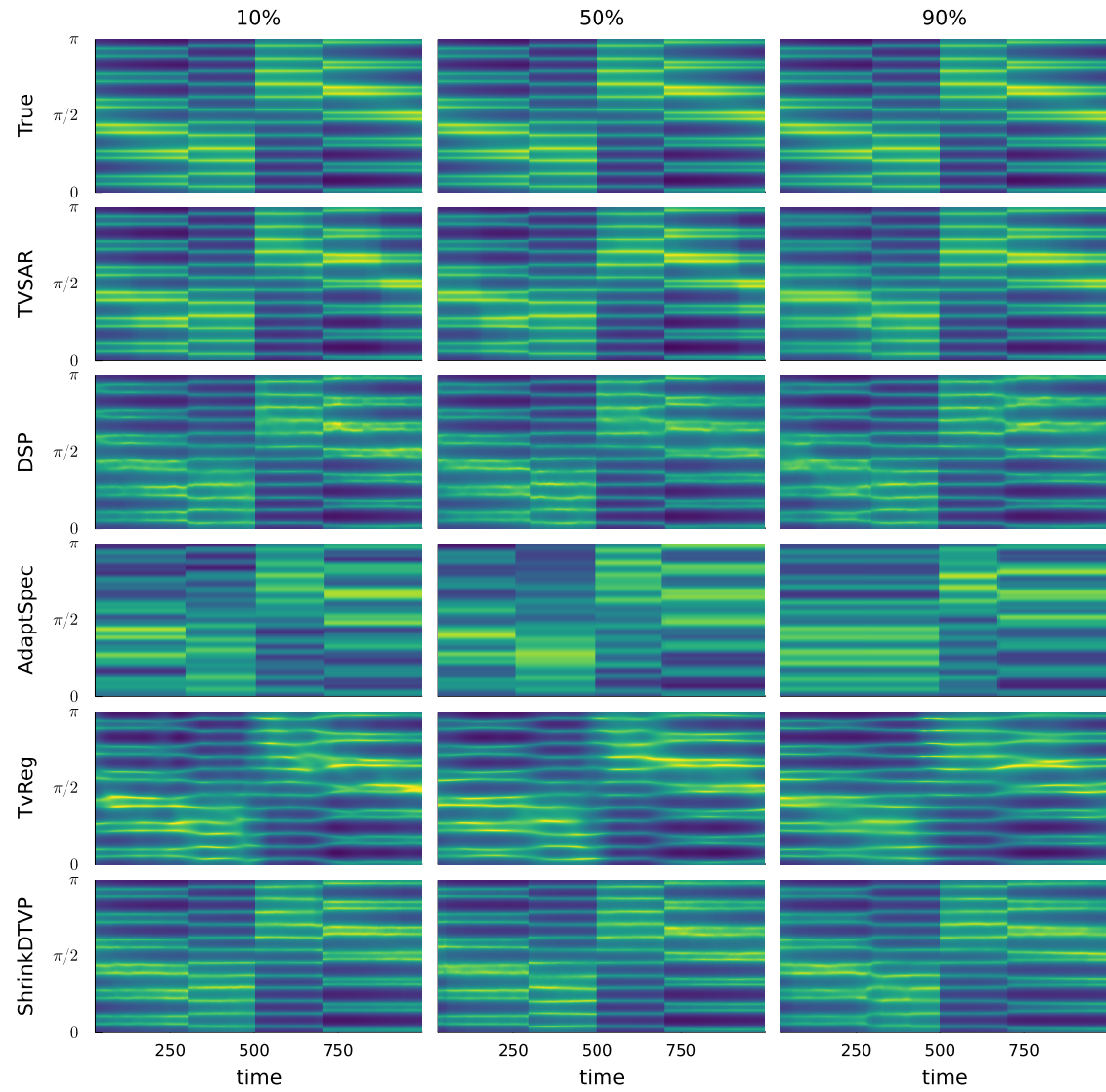


Figure 6: Experiment 1. Heatmaps of the estimated log spectral density over time for the different methods. The columns correspond to different datasets chosen from the percentiles of each model's MSE distribution, to show the performance of each model when it performs well (10%), average (50%) and poorly (90%).

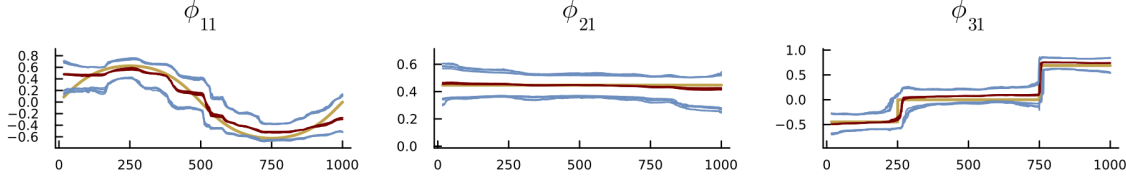


Figure 7: Experiment 2. Assessing MCMC convergence by re-estimating the model using the FFBS-x algorithm on the same dataset with five different initial values. The red and blue lines are posterior medians and 95% equal tail credible bands over time for each of the five repeated runs. The beige line is the true parameter evolution in the  $\phi$ -parameterization. See also Figure S12 for PGAS results with different number of particles.

results from PGAS(100) in Figure S12, showing that the extended Kalman filter is very accurate, even with both nonlinearities present in the model. Figures S12 and S14 also show that the posterior from the PGAS algorithm across different initial values is stabler compared to Experiment 1, but at least  $N = 50$  particles are necessary.

The right panel of Figure 5 displays box plots of the MSE for the log spectral density over 100 simulated datasets for Experiment 2. The TSVSAR model performs best, regardless of the sampling algorithm. The median MSE of AdaptSpec is approximately 0.33 (not shown in the figure). In contrast to Experiment 1, TvReg is now slightly better than DSP and ShrinkDTVP, which here perform similarly. The improved performance of TvReg is likely due to the smoother parameter trajectories in Experiment 2, which TvReg is known to handle well (Casas and Fernandez-Casal, 2019). The results in Section S5.3 in the supplementary material shows that the properties of the fitted spectral densities are qualitatively similar to the corresponding results in Experiment 1.

## 5 Application to US industrial production

We analyze monthly industrial production in the US between Jan 1919 - June 2024 from the FRED database (<https://fred.stlouisfed.org/series/INDPRO>); the left panel in Figure 8 shows the data, with the test data used for model selection in beige. To focus on the time-varying AR parameters, we log and detrend the data prior to the analysis by

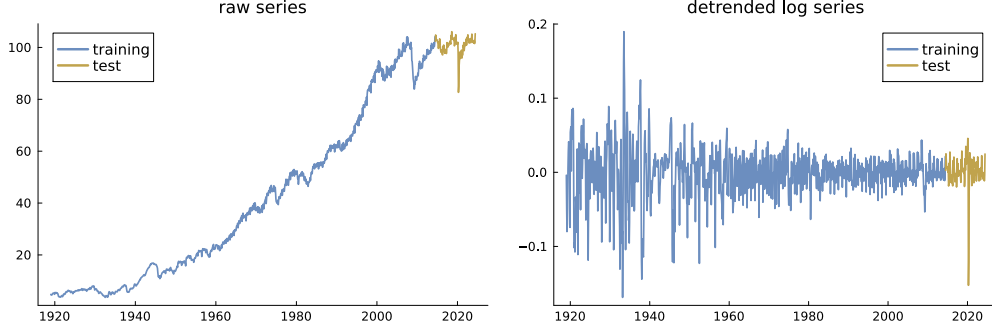


Figure 8: US industrial production time during Jan 1919 - June 2024. The test period used for model comparison, July 2014 - June 2024, is plotted in beige.

subtracting a local mean estimated with the `TvReg` package. The right panel of Figure 8 shows the detrended data. Following Kowal et al. (2019), we do not remove the time-varying variance of the data. Instead, we model the variance by a stochastic volatility component for  $\varepsilon_t$ , where the log-volatility  $g_t = \log \sigma_t^2$  is modeled as an AR(1) process

$$g_t = \mu_g + \kappa_g(g_{t-1} - \mu_g) + \zeta_t, \quad \zeta_t \stackrel{\text{iid}}{\sim} N(0, \sigma_\zeta^2). \quad (5.1)$$

The parameter path  $g_{1:T}$ , along with the global mean,  $\mu_g$ , the innovation variance,  $\sigma_\zeta^2$ , and the persistence of the log-volatility process,  $\kappa_g$ , are updated in separate Gibbs steps.

Given the monthly frequency of the data, we assume a seasonal period of  $s = 12$ , corresponding to an annual cycle. To determine a suitable number of regular lags  $p$  and seasonal lags  $P$ , Table 1 reports the out-of-sample log predictive score (LPS) for TVSAR models with different number of lags over the test period July 2014 - June 2024, with a total of 120 monthly observations. The most recent posterior distribution available at each time point is used when computing the predictive distribution; see Section S7 of the supplementary material for details on the LPS estimates. Note that this is a difficult period to forecast due to two massive outliers during the Covid-19 pandemic, which are here handled in-sample by the stochastic volatility part of the model, but are of course hard to forecast ahead of time. The TVSAR(1, 3)<sub>12</sub> model has the highest LPS, but the more parsimonious TVSAR(1, 2)<sub>12</sub> is within one LPS unit of the TVSAR(1, 3)<sub>12</sub> model and will therefore be used here for

	P = 1	P = 2	P = 3
p = 1	361.73	<i>365.99</i>	<b>366.82</b>
p = 2	360.85	362.08	364.89
p = 3	357.71	365.93	366.14

Table 1: Log predictive scores (LPS) for 1-step-ahead forecasts over the 120 months test period July 2014 - June 2024 in the US industrial production data. Averages across three separate runs. The model with largest LPS is in bold font and the most parsimonious model within 1 LPS of the model with highest LPS is shown in italic.

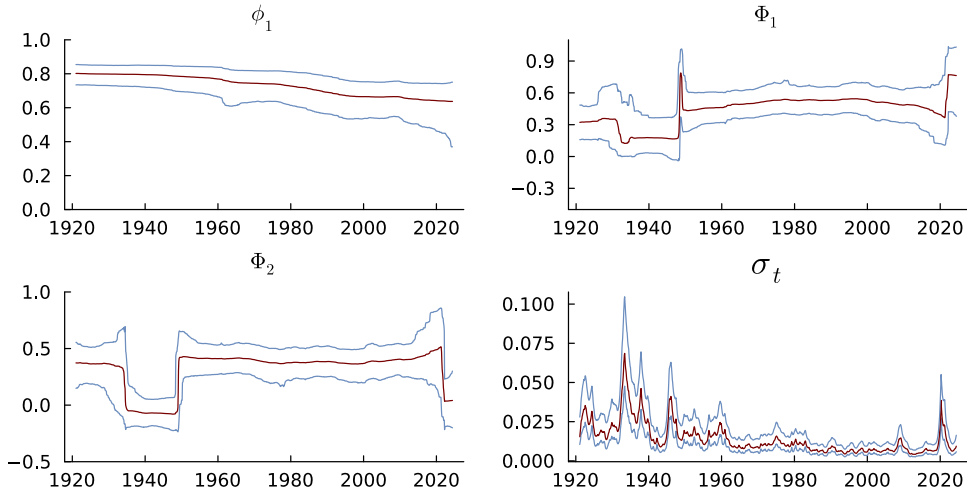


Figure 9: US industrial production. The posterior median and 95% credible intervals from the TVSAR(1, 2)<sub>12</sub> model with dynamic shrinkage prior and stochastic volatility, obtained with the FFBSx algorithm using an offset of  $10^{-16}$ .

illustration.

Figure 9 shows the posterior medians and 95% credible intervals for the AR coefficients in the TVSAR(1, 2)<sub>12</sub> model from 10 000 post burn-in draws obtained with the FFBSx algorithm. The regular AR coefficient in Figure 9 is stable over the century with only a mild downward trend. The two seasonal AR coefficients show substantial variation over time and jump to new levels during the Great Depression and WW2 period and the recent Covid-19 pandemic, while remaining very stable in the period in between these events. The posterior for the error standard deviation  $\sigma_t$  in the lower right panel of Figure 9 shows that there is a great deal of time-varying volatility in the data. Figure S29 shows that the FFBSx sampler has converged by plotting the posterior from three runs with different initial values

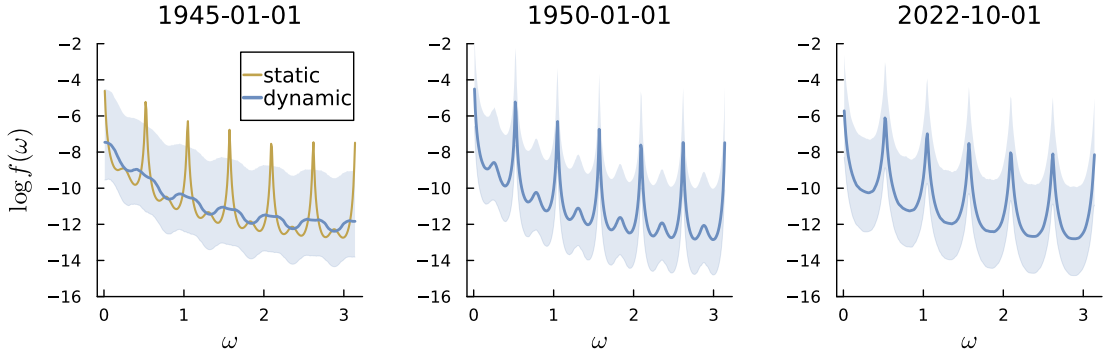


Figure 10: US industrial production. Fitted spectral density at three different time periods from TVSAR(1,2) model (blue line is posterior median and shaded regions are 95% credible intervals) and static parameters (beige line is posterior median). Both models have time-varying error variance. An interactive graph is available at <https://observablehq.com/@mattiasvillani/tvsar-spectral-usip>.

drawn from the prior. PGAS with 100 particles gives a similar posterior to FFBSx; see Figure S30.

Figure S32 in the supplementary material displays the posterior results from a TVSAR(1, 2)<sub>12</sub> model but with a traditional parameter evolution with homoscedastic Gaussian innovations. The results are qualitatively similar to the results from the dynamic shrinkage prior in Figure 9, but the parameter paths are much more wiggly in stable periods and oversmooth whenever there are jumps, a consequence of the constant parameter innovation variance.

Figures 10 and S31 plot time evolution of the log spectral density over time. The spectral density during the Great Depression and WW2 period has substantially less seasonal variation compared to other time periods, and the Covid-19 pandemic also stands out. Fitting a  $SAR(1, 2)_{12}$  with constant parameters gives posterior median estimates  $\hat{\phi}_1 = 0.759$ ,  $\hat{\Phi}_1 = 0.539$  and  $\hat{\Phi}_2 = 0.356$  and a fitted spectral density (beige line in Figure 10) dominated by the long stable period 1950-2020.

## 6 Conclusions

Our article proposes a time-varying multi-seasonal AR model with the parameters in the non-seasonal and the seasonal polynomials following the dynamic shrinkage process priors

in Kowal et al. (2019). We show empirically that the model can capture extended periods of constant parameters, periods of rapid changes and abrupt jumps, as well as shrinking redundant lags to zero. In every time period the freely evolving parameters are mapped to the AR parameter stability region to ensure that parameters do not drift into explosive regions. Our framework can be used with any of the recently developed global-local shrinkage priors, for example the prior processes in Kalli and Griffin (2014), Cadonna et al. (2020) and Knaus and Frühwirth-Schnatter (2023). The model allows for multiple seasonal periods, which is a common feature in modern datasets where data is often observed hourly or at even high frequencies. The seasonalities are modelled with the parsimonious multiplicative structure in Box et al. (2015).

Our Gibbs sampling algorithm samples from the joint posterior distribution of all the model parameters. The multiplicative model structure and the restriction to a stable process makes the model nonlinear and the update step for the time-varying AR parameters challenging. We propose the FFBsx sampler based on the extended Kalman filter. We show that this approximate sampler is accurate by comparing its posterior with PGAS (Lindsten et al., 2014), a state-of-the-art particle MCMC sampler which is known to be simulation consistent. The FFBsx sampler is fast, accurate and robust to the near-degeneracy in the state transition caused by the dynamic shrinkage process prior. The gradient in the FFBsx algorithm is efficiently computed by automatic differentiation, making it easy to write general computer code for any number of seasonal AR polynomials.

The model and inference method are explored in three simulated examples with different numbers of seasonalities, and shown to compare well to several benchmarks. An application to more than a century of monthly US industrial production data detects interesting and large changes in seasonality during the Great Depression and the recent Covid-19 pandemic, separated by a long period of remarkably constant seasonality.

There are several interesting directions for future research. First, the Gibbs sampling of  $\mathbf{h}_{0:T}$ ,  $\boldsymbol{\mu}$  and  $\boldsymbol{\kappa}$  can benefit from better mixing, for example using the interweaving strategy in

Yu and Meng (2011); Kastner and Frühwirth-Schnatter (2014). We have experimented with partial interweaving by sampling  $\boldsymbol{\mu}$  in both centered and non-centered parameterizations, but with limited success. Full interweaving is challenging since the  $T$  Pólya-Gamma variables needs to be sampled efficiently in the non-centered parameterization.

Second, as illustrated in Section S8, the FFBSx sampler for the TVSAR model with stability restrictions can give a distorted posterior distribution when the data generating process is close to the non-stable region for extended periods. We are currently exploring other FFBS posterior samplers for the TVSAR model based on several recently proposed Kalman-based approximate filters in the signal processing literature (Skoglund et al., 2015, 2019; García-Fernández et al., 2015) to get a more accurate posterior approximation in the near non-stable setting. See Section S8 for an example where the unscented Kalman filter (Julier and Uhlmann, 2004) improves on the FFBSx sampler based on the extended Kalman filter. We are also exploring other functions from the unrestricted parameters to the partial autocorrelations than the one used in this article, to improve the performance of the posterior samplers.

Third, several extensions of the TVSAR model should be developed. An extension of the model to the ARMA case with the exact likelihood function is already in progress. Given the good performance of the dynamic triple gamma prior as a linear benchmark model, it would also be interesting to compare the performance of the DSP and triple gamma priors in the TVSAR model. Extensions to multivariate seasonal vector AR and ARMA models are possible using the multivariate stability and invertibility restrictions in Ansley and Kohn (1986), but care is needed to handle the much larger number of parameters.

Finally, we also plan to explore the forecasting performance of the proposed model in a separate article, along with the potential interplay between time-varying AR parameters and a time-varying mean of the process.

## Acknowledgments

The authors thank the associate editor and two anonymous reviewers for many constructive comments that improved the manuscript.

## Funding

Mattias Villani was partially funded by the Swedish Research Council under Grant 2020-02846. The computations were enabled by resources provided by the National Academic Infrastructure for Supercomputing in Sweden (NAIIS), partially funded by the Swedish Research Council through grant agreement no. 2022-06725.

## Disclosure Statement

The authors report there are no competing interests to declare.

## References

Andrieu, C., Doucet, A., and Holenstein, R. (2010). Particle Markov chain Monte Carlo methods. *Journal of the Royal Statistical Society Series B*, 72(3):269–342.

Ansley, C. F. and Kohn, R. (1986). A note on reparameterizing a vector autoregressive moving average model to enforce stationarity. *Journal of Statistical Computation and Simulation*, 24(2):99–106.

Barndorff-Nielsen, O., Kent, J., and Sørensen, M. (1982). Normal variance-mean mixtures and z distributions. *International Statistical Review*, pages 145–159.

Barndorff-Nielsen, O. and Schou, G. (1973). On the parametrization of autoregressive models by partial autocorrelations. *Journal of Multivariate Analysis*, 3(4).

Baydin, A. G., Pearlmutter, B. A., Radul, A. A., and Siskind, J. M. (2018). Automatic differentiation in machine learning: a survey. *Journal of machine learning research*, 18(153):1–43.

Bertolacci, M. (2021). BayesSpec. <https://github.com/mbertolacci/BayesSpec.git>.

Bitto, A. and Frühwirth-Schnatter, S. (2019). Achieving shrinkage in a time-varying parameter model framework. *Journal of Econometrics*, 210(1):75–97.

Box, G. and Jenkins, G. M. (1970). *Time Series Analysis: Forecasting and Control*. San Francisco: Holden-Day, first edition.

Box, G. E., Jenkins, G. M., Reinsel, G. C., and Ljung, G. M. (2015). *Time series analysis: forecasting and control*. John Wiley & Sons, fifth edition.

Cadonna, A., Frühwirth-Schnatter, S., and Knaus, P. (2020). Triple the gamma—a unifying shrinkage prior for variance and variable selection in sparse state space and TVP models. *Econometrics*, 8(2):20.

Carter, C. K. and Kohn, R. (1994). On Gibbs sampling for state space models. *Biometrika*, 81(3):541–553.

Carvalho, C. M., Polson, N. G., and Scott, J. G. (2010). The horseshoe estimator for sparse signals. *Biometrika*, 97(2):465–480.

Casas, I. and Fernandez-Casal, R. (2019). *tvreg: Time-varying coefficients linear regression for single and multi-equations in r*. Technical report, SSRN. R package version 0.5.9.

Casas, I. and Fernandez-Casal, R. (2023). *tvReg: Time-Varying Coefficients Linear Regression for Single and Multi-Equations*. R package version 0.5.9.

Chib, S. (1998). Estimation and comparison of multiple change-point models. *Journal of econometrics*, 86(2):221–241.

Chopin, N. and Papaspiliopoulos, O. (2020). *An Introduction to Sequential Monte Carlo*. Springer.

Cogley, T. and Sargent, T. J. (2005). Drifts and volatilities: monetary policies and outcomes in the post wwii us. *Review of Economic dynamics*, 8(2):262–302.

Dahlhaus, R. (2000). A likelihood approximation for locally stationary processes. *The Annals of Statistics*, 28(6):1762–1794.

De Livera, A. M., Hyndman, R. J., and Snyder, R. D. (2011). Forecasting time series with complex seasonal patterns using exponential smoothing. *Journal of the American Statistical Association*, 106(496):1513–1527.

Everitt, R. G., Andrieu, C., and Davy, M. (2013). Online Bayesian inference in some time-frequency representations of non-stationary processes. *IEEE transactions on signal processing*, 61(22):5755–5766.

Frühwirth-Schnatter, S. (1994). Data augmentation and dynamic linear models. *Journal of time series analysis*, 15(2):183–202.

García-Fernández, Á. F., Svensson, L., Morelande, M. R., and Särkkä, S. (2015). Posterior linearization filter: Principles and implementation using sigma points. *IEEE transactions on signal processing*, 63(20):5561–5573.

Gerlach, R., Carter, C., and Kohn, R. (2000). Efficient Bayesian inference for dynamic mixture models. *Journal of the American Statistical Association*, 95(451):819–828.

Godsill, S. J., Doucet, A., and West, M. (2004). Monte Carlo smoothing for nonlinear time series. *Journal of the American Statistical Association*, 99(465):156–168.

Granger, C. W. and Joyeux, R. (1980). An introduction to long-memory time series models and fractional differencing. *Journal of time series analysis*, 1(1):15–29.

Hamilton, J. D. (1989). A new approach to the economic analysis of nonstationary time series and the business cycle. *Econometrica*, pages 357–384.

Hamilton, J. D. (1994). *Time series analysis*. Princeton university press.

Jones, M. C. (1987). Randomly choosing parameters from the stationarity and invertibility region of autoregressive-moving average models. *Journal of the Royal Statistical Society. Series C (Applied Statistics)*, 36(2):134–138.

Jones, M. C. and Faddy, M. (2003). A skew extension of the t-distribution, with applications. *Journal of the Royal Statistical Society Series B: Statistical Methodology*, 65(1):159–174.

Julier, S. J. and Uhlmann, J. K. (2004). Unscented filtering and nonlinear estimation. *Proceedings of the IEEE*, 92(3):401–422.

Kalli, M. and Griffin, J. E. (2014). Time-varying sparsity in dynamic regression models. *Journal of Econometrics*, 178(2):779–793.

Kastner, G. and Frühwirth-Schnatter, S. (2014). Ancillarity-sufficiency interweaving strategy (ASIS) for boosting MCMC estimation of stochastic volatility models. *Computational Statistics & Data Analysis*, 76:408–423.

Kim, S., Shephard, N., and Chib, S. (1998). Stochastic volatility: likelihood inference and comparison with arch models. *The review of economic studies*, 65(3):361–393.

Knaus, P., Bitto-Nemling, A., Cadonna, A., and Frühwirth-Schnatter, S. (2021). Shrinkage in the time-varying parameter model framework using the R package shrinkTVP. *Journal of Statistical Software*, 100(13).

Knaus, P. and Frühwirth-Schnatter, S. (2023). The dynamic triple gamma prior as a shrinkage process prior for time-varying parameter models. *arXiv preprint arXiv:2312.10487*.

Kowal, D. R., Matteson, D. S., and Ruppert, D. (2019). Dynamic shrinkage processes. *Journal of the Royal Statistical Society: Series B (Statistical Methodology)*, 81(4):781–804.

Lindsten, F., Bunch, P., Singh, S. S., and Schön, T. B. (2015). Particle ancestor sampling for near-degenerate or intractable state transition models. *arXiv preprint arXiv:1505.06356*.

Lindsten, F., Jordan, M. I., and Schon, T. B. (2014). Particle Gibbs with ancestor sampling. *Journal of Machine Learning Research*, 15:2145–2184.

Lindsten, F. and Schön, T. B. (2013). Backward simulation methods for Monte Carlo statistical inference. *Foundations and Trends in Machine Learning*, 6(1):1–143.

Makridakis, S. and Hibon, M. (1997). ARMA models and the Box–Jenkins methodology. *Journal of forecasting*, 16(3):147–163.

Monahan, J. F. (1984). A note on enforcing stationarity in autoregressive-moving average models. *Biometrika*, 71(2):403–404.

Omori, Y., Chib, S., Shephard, N., and Nakajima, J. (2007). Stochastic volatility with leverage: Fast and efficient likelihood inference. *Journal of Econometrics*, 140(2):425–449.

Piironen, J. and Vehtari, A. (2017). Sparsity information and regularization in the horseshoe and other shrinkage priors. *Electronic Journal of Statistics*, 11:5018–5051.

Polson, N. G. and Scott, J. G. (2010). Shrink globally, act locally: Sparse Bayesian regularization and prediction. *Bayesian statistics*, 9(501-538):105.

Polson, N. G., Scott, J. G., and Windle, J. (2013). Bayesian inference for logistic models using Pólya–gamma latent variables. *Journal of the American Statistical Association*, 108(504):1339–1349.

Prado, R. and West, M. (2010). *Time series: modeling, computation, and inference*. Chapman and Hall/CRC.

Rosen, O., Wood, S., and Stoffer, D. S. (2012). AdaptSPEC: Adaptive spectral estimation for nonstationary time series. *Journal of the American Statistical Association*, 107(500):1575–1589.

Rue, H. (2001). Fast sampling of Gaussian Markov random fields. *Journal of the Royal Statistical Society: Series B (Statistical Methodology)*, 63(2):325–338.

Skoglund, M. A., Gustafsson, F., and Hendeby, G. (2019). On iterative unscented kalman filter using optimization. In *2019 22th International Conference on Information Fusion (FUSION)*, pages 1–8. IEEE.

Skoglund, M. A., Hendeby, G., and Axehill, D. (2015). Extended Kalman filter modifications based on an optimization view point. In *2015 18th International Conference on Information Fusion (Fusion)*, pages 1856–1861. IEEE.

Smith, J. and Yadav, S. (1994). Forecasting costs incurred from unit differencing fractionally integrated processes. *International Journal of Forecasting*, 10(4):507–514.

Thrun, S., Burgard, W., and Fox, D. (2005). *Probabilistic robotics*. MA: MIT Press.

Wei, W. (2019). *Time Series Analysis Univariate and Multivariate Methods*. Pearson Modern Classics for Advanced Statistics Series. Pearson Education.

Wood, S., Rosen, O., and Kohn, R. (2011). Bayesian mixtures of autoregressive models. *Journal of Computational and Graphical Statistics*, 20(1):174–195.

Xie, T. and Ding, J. (2020). Forecasting with multiple seasonality. In *2020 IEEE International Conference on Big Data (Big Data)*, pages 240–245. IEEE.

Yang, W.-H., Holan, S., and Wikle, C. (2014). Bayesian lattice filters for time-varying autoregression and time-frequency analysis. *Bayesian Analysis*, 11.

Yu, Y. and Meng, X.-L. (2011). To center or not to center: That is not the question—an ancillarity-sufficiency interweaving strategy (asis) for boosting mcmc efficiency. *Journal of Computational and Graphical Statistics*, 20(3):531–570.

# Supplement to

## Time-Varying Multi-Seasonal AR Models

Ganna Fagerberg<sup>a\*</sup>, Mattias Villani<sup>a</sup> and Robert Kohn<sup>b,c</sup>

This Supplement contains proofs and additional results for the paper '*Time-Varying Multi-Seasonal AR Models*'.

### S1 Uniform distribution on the stability region

#### S1.1 Proof of Lemma 1

A random variable  $X \sim t_{\text{skew}}(a, b)$ , where  $a > 0$  and  $b > 0$  are parameters, follows the skew- $t$  distribution in Jones and Faddy (2003) if it has density

$$f(x) = \frac{1}{2^{a+b-1}B(a, b)\sqrt{a+b}} \left(1 + \frac{x}{\sqrt{a+b+x^2}}\right)^{a+1/2} \left(1 - \frac{x}{\sqrt{a+b+x^2}}\right)^{b+1/2}. \quad (\text{S1.1})$$

When  $a = b$ ,  $t_{\text{skew}}(a, b)$  reduces to the usual symmetric  $t$ -distribution with  $2a$  degrees of freedom. When  $a < b$ ,  $t_{\text{skew}}(a, b)$  is negatively skewed, while for  $a > b$  it is positively skewed.

---

\*Corresponding author: ganna.fagerberg@stat.su.se. <sup>a</sup>Department of Statistics, Stockholm University.

<sup>b</sup>School of Business, University of New South Wales. <sup>c</sup>Data Analytics Center for Resources and Environments (DARE).

One representation of this distribution is that if  $Y \sim \text{Beta}(a, b)$  then (Jones and Faddy, 2003)

$$X := \sqrt{a+b} \frac{2Y-1}{2\sqrt{Y(1-Y)}} \sim t_{\text{skew}}(a, b). \quad (\text{S1.2})$$

More generally,  $X \sim t_{\text{skew}}(a, b, \mu, \sigma)$  follows from a location-scale transformation  $X \rightarrow \mu + \sigma X$ .

Jones (1987) proves that if the partial autocorrelations are independently distributed as

$$r_k \sim \text{Beta}_{(-1,1)}(\alpha = \lfloor (k+1)/2 \rfloor, \beta = \lfloor k/2 \rfloor + 1), \quad (\text{S1.3})$$

where  $\lfloor x \rfloor$  is the integer part of  $x$ ,  $k = 1, \dots, p$ , and  $\text{Beta}_{(-1,1)}$  denotes the Beta distribution shifted to the interval  $(-1, 1)$ , then the implied distribution for the AR coefficients is uniform over the stability/stationary region in  $\phi$ -space.

Let  $q_k \sim \text{Beta}(\alpha_k = \lfloor (k+1)/2 \rfloor, \beta_k = \lfloor k/2 \rfloor + 1)$  follow the usual Beta distribution over  $(0, 1)$  so that, by definition,  $r_k \stackrel{d}{=} 2q_k - 1$ , where  $\stackrel{d}{=}$  denotes equality in distribution. Since  $r_k = \theta_k / \sqrt{1 + \theta_k^2}$ , we have

$$\theta_k = \frac{r_k}{\sqrt{1 - r_k^2}} \stackrel{d}{=} \frac{2q_k - 1}{\sqrt{1 - (2q_k - 1)^2}} = \frac{2q_k - 1}{2\sqrt{q_k(1 - q_k)}} = \frac{1}{\sqrt{k+1}} T$$

where

$$T = \sqrt{k+1} \frac{2q_k - 1}{2\sqrt{q_k(1 - q_k)}}$$

Since  $\alpha_k + \beta_k = k+1$  for all  $k$ , we have from (S1.2) that  $T \sim t_{\text{skew}}(\alpha_k, \beta_k)$ . This shows that  $\theta_k \sim t_{\text{skew}}(\alpha_k, \beta_k, 0, 1/\sqrt{k+1})$  for all  $k$ . When  $k$  is even, we have  $\alpha_k = k/2$  and  $\beta_k = (k+2)/2$ . When  $k$  is odd, we have  $\alpha_k = \beta_k$  and the skew-t distribution reduces to the symmetric student-t distribution with  $2\alpha_k = k+1$  degrees of freedom (Jones and Faddy, 2003), and hence  $\theta_k \sim t(k+1, 0, 1/\sqrt{k+1})$ , which proves the result in Lemma 1.

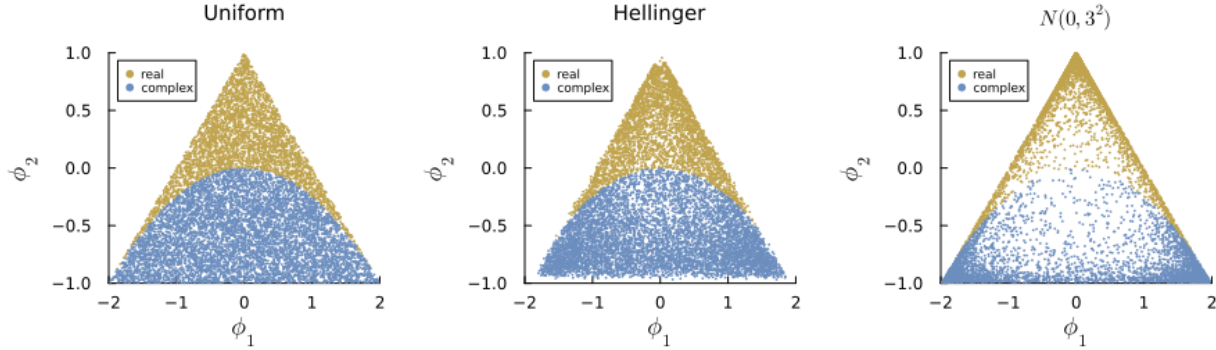


Figure S1: Illustrating 10 000 draws from the uniform distribution in Lemma 1 (left) and the optimal normal approximation in Table S1 (middle). The implied distribution from a  $N(0, 3^2)$  prior for both  $\theta_1$  and  $\theta_2$  is shown as reference (right). The beige points are draws with real roots in the AR polynomial while the blue points are draws with complex roots.

## S1.2 Normal approximation

The FFBs<sub>x</sub> algorithm requires a multivariate normal distribution for the initial state  $\boldsymbol{\theta}_0$ , or a mixture of multivariate normals if a more precise approximation is needed. We approximate the student-*t* and skew-*t* distributions in Lemma 1 by independent univariate normal distributions by finding the closest normal approximation to a *t* or skew *t* as measured by the Hellinger distance

$$H^2(p, q) = \frac{1}{2} \int_{\mathcal{X}} \left( \sqrt{p(x)} - \sqrt{q(x)} \right)^2 dx. \quad (\text{S1.4})$$

For the symmetric student-*t* case, we minimize with respect to the standard deviation, while for the skew-*t*, we minimize with respect to both the mean and standard deviation of the approximating normal. The optimal normal approximation is listed in Table S1 for up to 10 AR lags. Figure S1 shows that the implied distribution on the stability region from the normal approximation (middle) is close to the ideal uniform distribution (left). The right panel shows the implied distribution on  $\phi_1$  and  $\phi_2$  from a  $N(0, 3^2)$  distribution for each  $\theta_k$  as a reference, showing that this prior puts most of its mass close to the boundaries of the stability region.

	$\theta_1$	$\theta_2$	$\theta_3$	$\theta_4$	$\theta_5$	$\theta_6$	$\theta_7$	$\theta_8$	$\theta_9$	$\theta_{10}$
<b>mean</b>	0	-0.53	0	-0.264	0	-0.175	0	-0.13	0	-0.103
<b>stdev</b>	1.042	0.858	0.622	0.558	0.475	0.441	0.397	0.375	0.348	0.332

Table S1: Normal approximation of the student-t and skew-t distributions in Lemma 1 that minimizes the Hellinger distance.

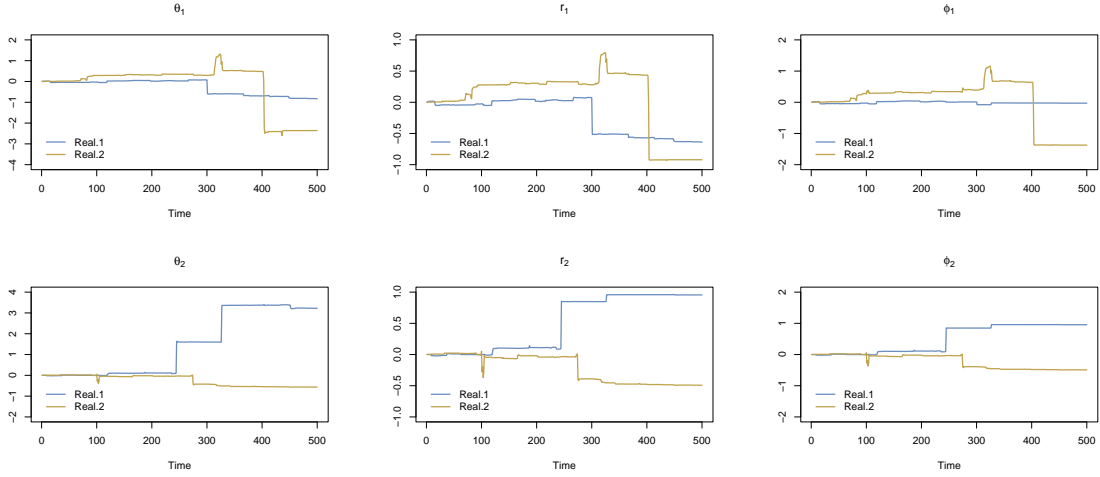


Figure S2: AR(2): Two realizations of time-varying trajectories for the unrestricted parameters  $\theta_1$  and  $\theta_2$  (left) following the DSP prior with global mean  $\mu = -15$ , the corresponding partial autocorrelations  $r_1$  and  $r_2$  (center), and the AR coefficients  $\phi_1$  and  $\phi_2$  (right). The persistence parameter is fixed at the prior mean  $\kappa = 0.5$  in the first realization and at  $\kappa = 0.8$  in the second realization.

## S2 Prior evolution of $\theta$ , $r$ and $\phi$

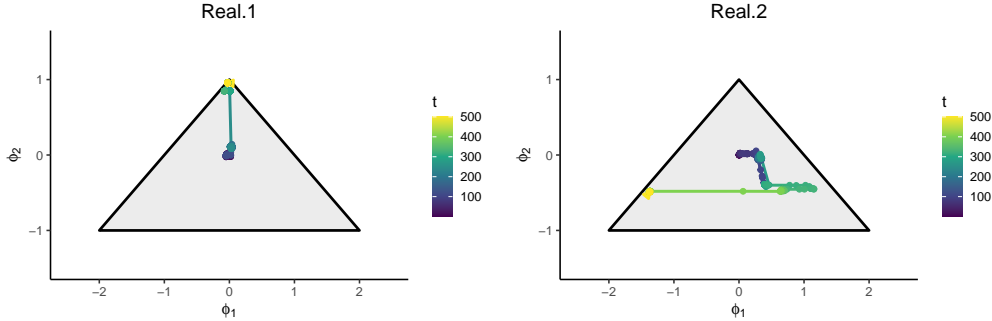


Figure S3: AR(2): The plots show the joint evolution of  $(\phi_1, \phi_2)$  within the stability region, indicated by the triangle, across Real.1 and Real.2.

## S3 Gibbs sampling updating steps

The Gibbs sampling algorithm is summarized in Algorithm S1. This section describes the updating steps for the parameters not covered in the main text. The updates are independent across parameters and will therefore be described for one parameter without the subscript  $k$ .

### S3.1 Updating the log volatility paths

Conditional on the static parameters  $\mu$  and  $\kappa$  and the parameter paths  $\theta_{0:T}$ , the sampling step for stochastic volatility models in Rue (2001) and Kastner and Frühwirth-Schnatter (2014) can be used to efficiently sample the  $r$  columns of  $\mathbf{h}_{0:T}$  independently from multivariate normal distributions with a tri-diagonal covariance matrix. Since the log-volatilities for different parameters are drawn independently, we focus on one parameter and drop the subscript  $k$  and write  $h_t$  for the rest of this subsection. The updating step for  $\mathbf{h}_{0:T}$  is the same as in Kowal et al. (2019) and is given here to explain the role of the Pólya-Gamma variables in Algorithm S1. The updating of  $\mu$  and  $\kappa$  are slightly different from Kowal et al. (2019) due to different priors.

The sampling of  $h_{0:T}$  in Kowal et al. (2019) follows the log-volatility estimation in Kim

---

**Algorithm S1:** Gibbs sampling from joint posterior  $p(\boldsymbol{\theta}_{0:T}, \mathbf{h}_{0:T}, \sigma_{1:T}, \boldsymbol{\mu}, \boldsymbol{\kappa} | y_{1:T})$ 


---

**Input:** data  $y_{1:T}$

initial  $\mu^{(0)}$ , defaulting to  $(\mu_0, \dots, \mu_0)^\top$ , where  $\mu_0$  is the prior mean  
 initial  $\kappa^{(0)}$ , defaulting to  $(\kappa_0, \dots, \kappa_0)^\top$ , where  $\kappa_0$  is the prior mean  
 initial  $\mathbf{h}_{1:T}^{(0)}$ , defaulting to  $h_{kt}^{(0)} = \mu_0$  for all  $k, t$   
 initial  $\sigma_{1:T}^{(0)}$ , defaulting to an estimate from the static seasonal AR  
 initial Pólya-Gamma variables  $\boldsymbol{\xi}_{0:T}^{(0)}$ , defaulting to 1 for all  $k, t$   
 tuning parameters for PGAS  
 the number of posterior draws  $J$

Run the particle filter to compute initial reference trajectory  $\boldsymbol{\theta}_{0:T}^{(0)}$  for PGAS

**for**  $j = 1$  **to**  $J$  **do**

  \\ draw the parameter evolutions using PGAS or FFBsX  
 $\boldsymbol{\theta}_{0:T}^{(j)} \leftarrow \text{PGAS/FFBSX}(\boldsymbol{\theta}_{0:T} | \mathbf{h}_{0:T}^{(j-1)}, \sigma_{1:T}^{(j-1)}, y_{1:T}, \boldsymbol{\theta}_{0:T}^{(j-1)})$

  \\ draw the error standard deviations

$\boldsymbol{\sigma}_{1:T}^{(j)} \leftarrow p(\boldsymbol{\sigma}_{1:T} | \boldsymbol{\theta}_{0:T}^{(j)}, y_{1:T})$

**for**  $k = 1$  **to**  $r$  **do in parallel**

    \\ draw mixture of normals allocations

$\mathbf{a}_{k,1:T}^{(j)} \leftarrow p(\mathbf{a}_{k,1:T} | \boldsymbol{\theta}_{k,0:T}^{(j)}, h_{k,0:T}^{(j-1)})$

    \\ draw log-volatilities

$\mathbf{h}_{k,0:T}^{(j)} \leftarrow p(\mathbf{h}_{k,0:T} | \boldsymbol{\theta}_{k,0:T}^{(j)}, \mathbf{a}_{k,1:T}^{(j)}, \kappa_k^{(j-1)}, \mu_k^{(j-1)}, \boldsymbol{\xi}_{k,1:T}^{(j-1)})$

    \\ draw Pólya-Gamma variables

$\boldsymbol{\xi}_{k,0:T}^{(j)} \leftarrow p(\boldsymbol{\xi}_{k,0:T} | \mathbf{h}_{k,0:T}^{(j)}, \kappa_k^{(j-1)}, \mu_k^{(j-1)})$

    \\ draw global mean log-volatility

$\mu_k^{(j)} \leftarrow p(\mu_k | \mathbf{h}_{k,1:T}^{(j)}, \kappa_k^{(j-1)}, \boldsymbol{\xi}_{k,1:T}^{(j)})$

    \\ draw global log-volatility persistence

$\kappa_k^{(j)} \leftarrow p(\kappa_k | \mathbf{h}_{k,1:T}^{(j)}, \mu_k^{(j)}, \boldsymbol{\xi}_{k,1:T}^{(j)})$

**end**

**end**

**Output:** draws from the joint posterior of  $\boldsymbol{\theta}_{0:T}, \mathbf{h}_{0:T}, \sigma_{1:T}, \boldsymbol{\mu}$  and  $\boldsymbol{\kappa}$ .

---

et al. (1998) where the model for the parameter innovations  $\nu_t = \theta_t - \theta_{t-1}$

$$\nu_t = \exp(h_t/2)\epsilon_t, \quad \epsilon_t \stackrel{\text{iid}}{\sim} N(0, 1) \quad (\text{S3.1})$$

is rewritten by squaring and taking logs on both sides

$$\log \nu_t^2 = h_t + \log \epsilon_t^2, \quad (\text{S3.2})$$

so that  $h_t$  becomes an additive term. The error term  $\log \epsilon_t^2$  is however  $\log \chi_1^2$ -distributed, which Kim et al. (1998) solves by approximating the  $\log \chi_1^2$  distribution with a mixture of normals, thereby turning the model into a Gaussian model conditional on the latent mixture allocation variables  $a_{1:T}$ ; we use the 10-component mixture in Omori et al. (2007).

The prior for the log-volatility  $h_{0:T}$  series follows the dynamic shrinkage process

$$h_t = \mu + \kappa(h_{t-1} - \mu) + \eta_t, \quad \eta_t \stackrel{\text{iid}}{\sim} Z(1/2, 1/2, 0, 1), \text{ for } t = 1, \dots, T, \quad (\text{S3.3})$$

with initial condition  $h_0 = \mu + \eta_0$  and  $\eta_0 \sim Z(1/2, 1/2, 0, 1)$ . Kowal et al. (2019) show that the prior can be augmented with Pólya-Gamma variables  $\xi_{0:T}$  to become conditionally Gaussian

$$\begin{aligned} h_t &= \mu + \kappa(h_{t-1} - \mu) + \eta_t \\ \eta_t | \xi_t &\stackrel{\text{iid}}{\sim} N(0, \xi_t^{-1}) \\ \xi_t &\stackrel{\text{iid}}{\sim} \text{PG}(1, 0), \end{aligned} \quad (\text{S3.4})$$

where PG is the Pólya-Gamma distribution (Polson et al., 2013). Now, conditional on the mixture allocation  $a_{1:T}$  and the Pólya-Gamma variables  $\xi_{0:T}$ , Kowal et al. (2019) combine the conditionally Gaussian likelihood from (S3.2) with the conditionally Gaussian prior process in (S3.4) to derive the posterior of  $\mathbf{h}_{0:T}$  as multivariate normal. The inverse covariance matrix

is tri-diagonal, which can be elegantly exploited for efficient sampling, see Rue (2001) and Kowal et al. (2019) for details.

To avoid numerical issues it is common to add some small positive offset before taking logs in (S3.2)

$$\log(\nu_t^2 + \text{offset}) = h_t + \log \epsilon_t^2, \quad (\text{S3.5})$$

With  $\nu_t$  being the change in the parameter corresponding to  $h_t$ , this offset turns out to be important here since the dynamic shrinkage prior encourages parameters to remain constant for extended periods, so  $\nu_t$  tends to be close to zero for some  $t$ . The `dsp` package in R that accompanies Kowal et al. (2019) uses a different offset for each parameter and in each Gibbs sampling iteration following the rule

$$\text{offset} = \begin{cases} \max(10^{-8}, 10^{-6} \cdot \text{mad}(\nu_{1:T})) & \text{if } \nu_t^2 < 10^{-16} \text{ for any } t \\ 0 & \text{otherwise,} \end{cases} \quad (\text{S3.6})$$

where  $\text{mad}(\boldsymbol{x})$  is the median absolute deviation for the elements in the vector  $\boldsymbol{x}$ . Section 4 further discusses the effect of the offset.

## S3.2 Updating $\kappa$

The full conditional posteriors of the  $\kappa_k$  are independent and we now give the distribution for a typical element  $\kappa$  of  $\boldsymbol{\kappa}$  conditional on its log-volatility process, which we denote by the generic  $h_{0:T}$ . The relevant part of the model for updating one of the  $\kappa$  parameters is the Pólya-Gamma augmented model in (S3.4).

Conditioning on the Pólya-Gamma variables  $\xi_{0:T}$ , the parameter  $\kappa$  is the regression coefficient in a heteroscedastic Gaussian regression model. Multiplying both sides of  $h_t = \mu + \kappa(h_{t-1} - \mu) + \eta_t$  in (S3.4) by  $\xi_t^{1/2}$  makes the model homoscedastic and a standard derivation for

Bayesian linear regression shows that the full conditional posterior is

$$\kappa | \mu, \xi_{0:T}, h_{0:T} \sim \text{TN}(\kappa_T, \psi_T^2, -1, 1) \quad (\text{S3.7})$$

where  $\psi_T^{-2} = \tilde{\mathbf{h}}_{-1}^\top \tilde{\mathbf{h}}_{-1} + \psi_0^{-2}$ ,  $\kappa_T = w\hat{\kappa} + (1-w)\kappa_0$ ,  $\hat{\kappa} = (\tilde{\mathbf{h}}_{-1}^\top \tilde{\mathbf{h}}_{-1})^{-1} \tilde{\mathbf{h}}_{-1}^\top \tilde{\mathbf{h}}$ ,  $w = \frac{\tilde{\mathbf{h}}_{-1}^\top \tilde{\mathbf{h}}_{-1}}{\tilde{\mathbf{h}}_{-1}^\top \tilde{\mathbf{h}}_{-1} + \psi_0^{-2}}$ , using the notation  $\tilde{\mathbf{h}} = (\tilde{h}_1, \dots, \tilde{h}_T)^\top$  and  $\tilde{\mathbf{h}}_{-1} = (\tilde{h}_0, \dots, \tilde{h}_{T-1})^\top$ .

### S3.3 Updating $\mu$

The full conditional posteriors for the elements in  $\boldsymbol{\mu}$  are independent and we will describe the updating step for one such generic element  $\mu$ . We can rewrite the model in (S3.4) as

$$z_t = \mu + \tilde{\eta}_t \quad (\text{S3.8})$$

where

$$z_t = \frac{h_t - \kappa h_{t-1}}{1 - \kappa}, \quad (\text{S3.9})$$

$$\tilde{\eta}_t = \eta_t / (1 - \kappa) \sim N\left(0, \tilde{\xi}_t^{-1}\right) \quad (\text{S3.10})$$

with  $\tilde{\xi}_t = (1 - \kappa)^2 \xi_t$  and  $z_0 = h_0 = \mu + \eta_0$  with  $\eta_0 \sim N(0, \xi_t^{-1})$ . This shows that  $\mu$  is the mean of the transformed data  $z_t$ . A standard derivation of the posterior of a mean in a Gaussian model with known heteroscedastic variances shows that

$$\mu | \kappa, \xi_{0:T}, h_{0:T} \sim N(\mu_T, \sigma_T^2), \quad (\text{S3.11})$$

where  $\sigma_T^{-2} = \sum_{t=0}^T \tilde{\xi}_t + \sigma_0^{-2}$  and  $\mu_T = v\hat{\mu} + (1-v)\mu_0$  with

$$v = \frac{\sum_{t=0}^T \tilde{\xi}_t}{\sum_{t=0}^T \tilde{\xi}_t + \sigma_0^{-2}}. \quad (\text{S3.12})$$

### S3.4 Updating the $\log \chi_1^2$ mixture allocation $a_{1:T}$

This is a standard step based on the 10-component mixture in Omori et al. (2007); see Kowal et al. (2019) for details.

### S3.5 Updating $\xi_{1:T}$

The updating of the Pólya-Gamma variables is identical to the update in Kowal et al. (2019).

### S3.6 Updating the observational noise variance

For the static variance case we use the conjugate prior  $\sigma^2 \sim \text{Inv-}\chi^2(v_0, s_0^2)$ , the scaled inverse chi-square distribution. The posterior distribution is  $\text{Inv-}\chi^2(v_T, s_T^2)$ , with  $v_T = v_0 + T$  and  $s_T^2 = (v_0 s_0^2 + \sum_{i=1}^T \hat{\epsilon}_t^2) / (v_0 + T)$ .

In the time-varying error variance case, we follow Kowal et al. (2019) and use a stochastic volatility (SV) model with the updating step in Kastner and Frühwirth-Schnatter (2014), similarly to the sampling of  $h_{kt}$  in Section S3.1.

## S4 Particle Gibbs with Ancestor Sampling

A general SSM with state vector  $\boldsymbol{\theta}_t$  and measurements  $y_t$  is of the form

$$\boldsymbol{\theta}_0 \sim f_0(\boldsymbol{\theta}_0), \quad \boldsymbol{\theta}_t \sim f(\boldsymbol{\theta}_t | \boldsymbol{\theta}_{t-1}), \quad y_t \sim g(y_t | \boldsymbol{\theta}_t), \quad (\text{S4.1})$$

where  $f_0$  is the initial prior,  $f(\boldsymbol{\theta}_t | \boldsymbol{\theta}_{t-1})$  is the state transition model and  $g(y_t | \boldsymbol{\theta}_t)$  is the measurement model.

Particle filters approximate the target filtering distribution,  $p(\boldsymbol{\theta}_t | y_{1:t})$  by a set of  $N$  weighted particles,  $\{\boldsymbol{\theta}_t^i, w_t^i\}_{i=1}^N$

$$\widehat{p}(\boldsymbol{\theta}_t | y_{1:t}) = \sum_{i=1}^N w_t^i \delta_{\boldsymbol{\theta}_t^i}(\boldsymbol{\theta}_t), \quad (\text{S4.2})$$

where  $\sum_i w_t^i = 1$  and  $\delta(\cdot)$  is the point mass Dirac delta function. The particles evolve in time based on a Markov proposal density  $q_t(\boldsymbol{\theta}_t | \boldsymbol{\theta}_{t-1}, y_t)$  and are assigned importance weights

$$w_t^i \propto \frac{g(y_t | \boldsymbol{\theta}_t^i) f(\boldsymbol{\theta}_t^i | \boldsymbol{\theta}_{t-1}^i)}{q_t(\boldsymbol{\theta}_t^i | \boldsymbol{\theta}_{t-1}^i, y_t)} w_{t-1}^i, \quad (\text{S4.3})$$

where  $g(y_t | \boldsymbol{\theta}_t)$  is the measurement density and  $f(\boldsymbol{\theta}_t | \boldsymbol{\theta}_{t-1})$  is the transition density. The particles at step  $t$  are resampled with replacement with probabilities proportional to  $w_t^i$  to form an unweighted sample from the filtering distribution  $p(\boldsymbol{\theta}_t | y_{1:t})$ . The bootstrap particle filter uses the model's transition density  $f(\boldsymbol{\theta}_t | \boldsymbol{\theta}_{t-1})$  as a proposal and the importance weights in (S4.3) simplify to

$$w_t^i \propto g(y_t | \boldsymbol{\theta}_t^i) w_{t-1}^i. \quad (\text{S4.4})$$

The resampling step can be expressed as the sampling of ancestor indexes,  $a_t^i$ , where the outcome  $a_t^i = j$  means that the  $i$ th particle at time  $t$  is propagated from the  $j$ th particle at time  $t-1$  (Andrieu et al., 2010).

Particle filters often face degeneracy problems with only a few particles carrying significant weight. The resampling step partially addresses this problem, but frequent resampling can lead to a loss of particle diversity. To address this, it is common to resample only when the estimated effective sample size

$$\text{ESS}_{t-1} := \frac{1}{\sum_{i=1}^N (w_{t-1}^i)^2} \quad (\text{S4.5})$$

is below a certain threshold  $\text{ESS}_{\min}$ . We use  $\text{ESS}_{\min} = N/2$  and systematic resampling (Chopin and Papaspiliopoulos, 2020, Ch. 9) as default settings.

Andrieu et al. (2010) introduce particle MCMC (PMCMC) methods that combine MCMC and SMC. One such PMCMC sampler is the particle Gibbs sampler that uses a particular conditional SMC update. This update is similar to the usual SMC approximation, but is conditioned on a prespecified reference trajectory  $\boldsymbol{\theta}_{0:T}^*$  that is ensured to survive all

resampling steps. Andrieu et al. (2010) show that conditioning on the reference trajectory makes the update a valid Markov kernel that leaves the conditional posterior  $p(\boldsymbol{\theta}_{0:T}|y_{1:T}, \cdot)$  invariant, and can therefore be used in a Gibbs sampling step.

---

**Algorithm S2:** PGAS Markov kernel for  $p(\boldsymbol{\theta}_{0:T}|y_{1:T})$ 


---

**Input:** data  $y_{1:T}$ , reference trajectory  $\boldsymbol{\theta}_{0:T}^*$ , number of particles  $N$ , initial proposal distribution  $q_0(\boldsymbol{\theta}_0)$  and resampling threshold  $\text{ESS}_{\min}$ .

```

\\ t = 0
 $\boldsymbol{\theta}_0^i \sim q_0(\boldsymbol{\theta}_0)$  for  $i = 1, \dots, N - 1$ 
 $\boldsymbol{\theta}_0^N = \boldsymbol{\theta}_0^*$ 
 $w_0^i \propto \frac{f_0(\boldsymbol{\theta}_0^i)}{q_0(\boldsymbol{\theta}_0^i)}$  for  $i = 1, \dots, N$ 

for  $t = 1$  to  $T$  do
    \\ resample
    if  $\text{ESS}_{t-1} < \text{ESS}_{\min}$  then
        draw  $a_t^i$  with  $P(a_t^i = j) \propto w_{t-1}^j$  for  $i = 1, \dots, N - 1$ 
        \\ sample the ancestor of reference particle
        draw  $a_t^N$  with  $P(a_t^N = j) \propto w_{t-1}^j f(\boldsymbol{\theta}_t^* | \boldsymbol{\theta}_{t-1}^j)$ 
        set  $w_{t-1}^i = \frac{1}{N}$  for  $i = 1, \dots, N$ 
    else
        | set  $a_t^i = i$  for  $i = 1, \dots, N$ 
    end

    \\ propagate the particles forward one step
    draw  $\boldsymbol{\theta}_t^i \sim f(\boldsymbol{\theta}_t^i | \boldsymbol{\theta}_{t-1}^{a_t^i})$  for  $i = 1, \dots, N - 1$ 
    set  $\boldsymbol{\theta}_t^N = \boldsymbol{\theta}_t^*$ 
    set  $\boldsymbol{\theta}_{1:t}^i = \{\boldsymbol{\theta}_{1:t-1}^{a_t^i}, \boldsymbol{\theta}_t^i\}$  for  $i = 1, \dots, N$ 

    \\ compute the importance weights
     $w_t^i \propto w_{t-1}^i g(y_t | \boldsymbol{\theta}_t^i)$  for  $i = 1, \dots, N$ 

end
Draw  $J$  with  $P(J = i) \propto w_T^i$ 
return  $\boldsymbol{\theta}_{0:T}^J$ 

```

---

The particle Gibbs sampler can mix poorly due to path degeneracy in the underlying SMC sampler. The Particle Gibbs with Ancestor Sampling (PGAS) algorithm in Lindsten et al. (2014) improves the mixing by sampling the ancestor of the reference trajectory at each time

$t$  based on the ancestor weights

$$\tilde{w}_{t-1|T}^i \propto w_{t-1}^i f(\boldsymbol{\theta}_t^* | \boldsymbol{\theta}_{t-1}^i) \text{ for } i = 1, \dots, N, \quad (\text{S4.6})$$

in the special case of Markovian SSMs using the bootstrap filter. Lindsten et al. (2014) show that the ancestral sampling step does not compromise the validity of the Markov kernel, and can greatly improve mixing, even with few particles. The PGAS algorithm approximates the joint smoothing density with a single forward sweep, unlike other methods that often require explicit forward and backward sweeps (Lindsten and Schön, 2013). Algorithm S2 summarizes the PGAS sampler with the bootstrap filter, and we refer to Lindsten et al. (2014) for further details.

The initial proposal distribution  $r_0(\boldsymbol{\theta}_0)$  is often taken as the prior  $f_0(\boldsymbol{\theta}_0)$ , but we find it useful for faster convergence to instead use the smoothing posterior at  $t = 0$  from a short (500 draws) preliminary run of the approximate FFBSx described in the main article.

The PGAS algorithm can suffer from particle degeneracy in near-degenerate models (Lindsten et al., 2015), for example when the innovations in the transition model have close to zero variance for some  $t$ . A potential solution is to rejuvenate both the ancestors and the reference trajectory itself; see Lindsten et al. (2015) in the context of PGAS. However, we find that these modifications require careful adjustments to suit our specific model, indicating that further research is needed to adapt them effectively. We instead develop an approximate sampling step that replaces the Kalman filter in the FFBS sampler with the extended Kalman filter (EKF), as explained in our article.

## S5 Additional details and results from the simulation experiments

### S5.1 Experiment 1

The first experiment simulates data from the time-varying TVSAR(2, 2)<sub>12</sub>

$$(1 - \phi_{1t}L - \phi_{2t}L^2)(1 - \Phi_{1t}L^{12} - \Phi_{2t}L^{24})y_t = \varepsilon_t, \quad (\text{S5.1})$$

where  $\varepsilon_t \sim N(0, 1)$ .

The time evolution of the unrestricted non-seasonal parameters is

$$\theta_{1t} = \begin{cases} 0.8 \sin\left(\frac{\pi t}{T}\right) & \text{for } t = 1, \dots, 500 \\ -0.8 \sin\left(\frac{\pi t}{T}\right) & \text{for } t = 501, \dots, 1000 \end{cases} \quad \theta_{2t} = -0.8 \text{ for all } t. \quad (\text{S5.2})$$

and the time evolution of the unrestricted seasonal parameters is

$$\Theta_{1t} = \begin{cases} -0.70 & \text{for } t = 1, \dots, 300 \\ 0 & \text{for } t = 301, \dots, 700 \\ 0.95 & \text{for } t = 701, \dots, 1000 \end{cases} \quad \Theta_{2t} = -0.9 \text{ for all } t. \quad (\text{S5.3})$$

The left graph of Figure S4 shows the time evolution of the eigenvalues of the companion matrix for the regular AR polynomial

$$\begin{pmatrix} \phi_{1t} & \phi_{2t} & \cdots & \phi_{pt} \\ \mathbf{I}_{p-1} & \mathbf{0}_{p-1} \end{pmatrix}. \quad (\text{S5.4})$$

The right graph of Figure S4 shows the time evolution of the eigenvalues of the companion matrix for the seasonal AR polynomial.

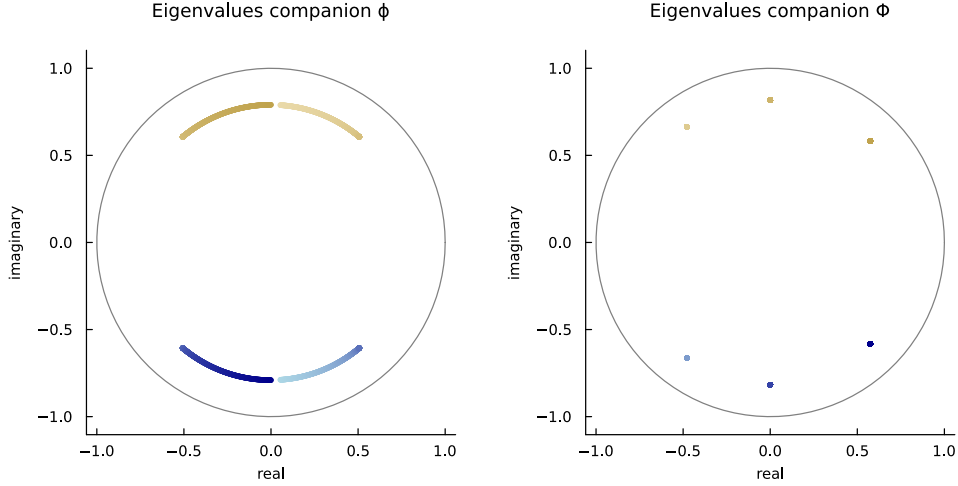


Figure S4: Experiment 1. Eigenvalues for the companion matrix of the regular and seasonal polynomials over time for the data generating process. The color scale for the eigenvalues represents time, with darker colors indicating later points in the time sequence.

FFBSx-m			FFBSx-l			PGAS(100)					
	$\pi/4$	$\pi/2$	$3\pi/4$		$\pi/4$	$\pi/2$	$3\pi/4$		$\pi/4$	$\pi/2$	$3\pi/4$
$t = 100$	377	330	460		506	475	533		38	35	41
$t = 400$	418	454	436		548	620	595		167	216	179
$t = 800$	375	412	361		418	534	474		324	412	348

Table S2: Experiment 1. Effective sample size (ESS) for estimating the spectral density for three algorithms. ESS for the spectral density is computed at three selected time points (rows) and at three selected frequencies (columns). The ESS is from an initial posterior sample of 10 000 draws thinned down to 1000 draws. An offset of  $10^{-16}$  is used.

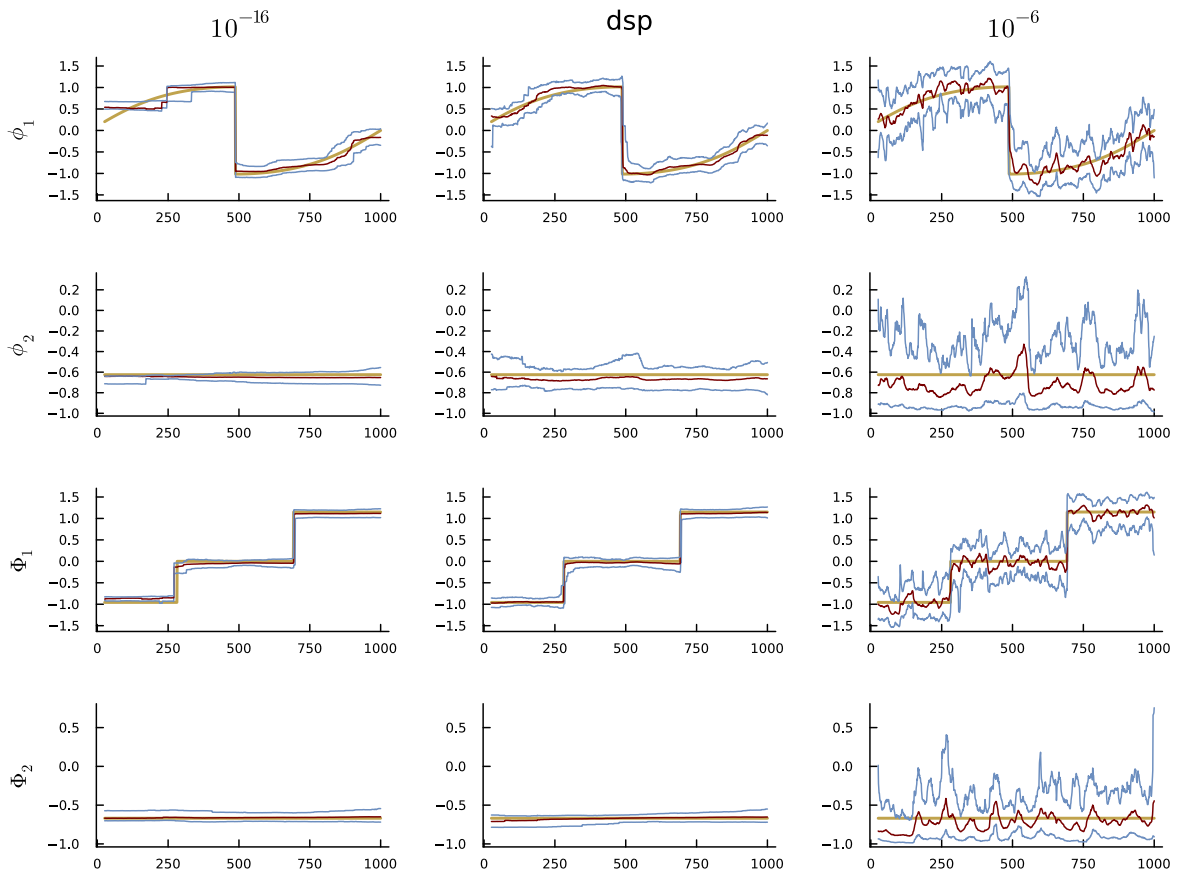


Figure S5: Experiment 1. Posterior median and 95% credible intervals from PGAS(100) from one run for the three different offsets in the log-volatility model for  $\mathbf{h}_t$

Figure S6 gives an alternative view to the heatmaps in Figure 6 by plotting the estimated time-evolution at some selected frequencies. Figure S7 plots the fitted log spectral densities at three different time points, again showing the fit for three different datasets selected from the MSE percentiles for each method. Clearly, our TVSAR model gives less wiggly fits than DSP, while TvReg oversmooths.

For completeness, we also compare the performance of the TVSAR model with a SARMA model with time invariant parameters in this experiment. Figure 5 does not show the MSE for this model, but it does, as expected, perform very poorly with a median MSE of 5.22. The static SARMA model is fitted with `auto.arima` in the `forecast` package in R, which automatically determines the optimal AR and MA lag orders; we allow for a maximal order of 5 for all regular and seasonal lags.

## S5.2 Experiment 1 - one lag version

In this experiment, data is simulated from the following one-lag restricted version of the DGP in Experiment 1, a time-varying TVSAR( $\mathbf{s}, \mathbf{p}$ ) with  $\mathbf{s} = (1, 12)$  and  $\mathbf{p} = (1, 1)$ ,

$$(1 - \phi_{1t}L)(1 - \Phi_{1t}L^{12})y_t = \varepsilon_t, \quad (\text{S5.5})$$

where  $\varepsilon_t \sim N(0, 1)$ . The time evolution of the parameters are the same as for the first regular and seasonal lag in Experiment 1. Figure S8 shows the time evolution of the eigenvalues of the companion matrix of the regular and seasonal AR coefficients.

Figures S9 and S10 show that PGAS converges much faster than for the SAR(2,2) model in Experiment 1, even for an offset of  $10^{-16}$ .

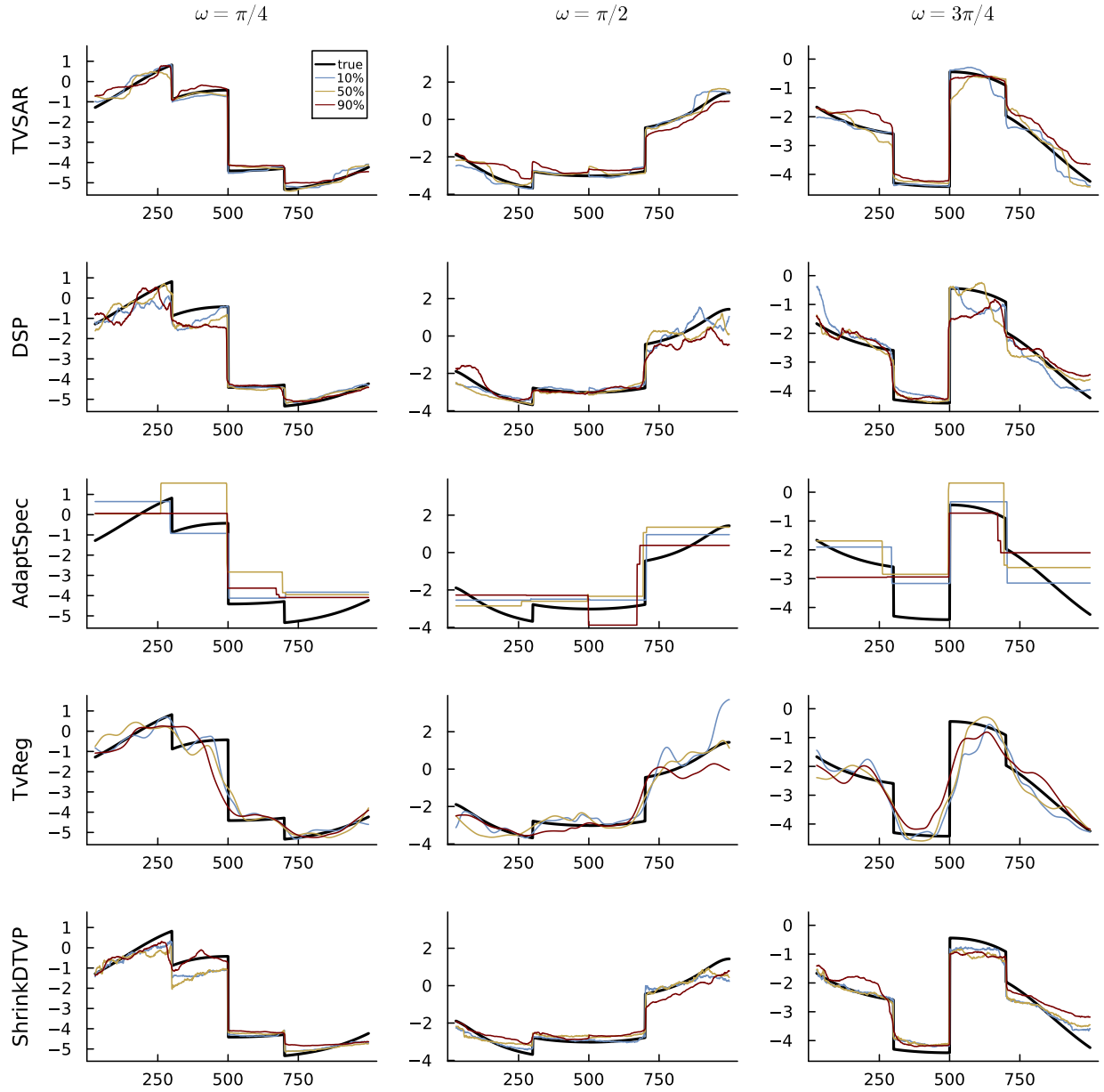


Figure S6: Experiment 1. Time evolution of the log spectral density at three different frequencies (columns) for several different models (rows). The black line is the true spectral density and the three colored lines are the posterior median estimates from three different datasets chosen from the MSE percentiles.

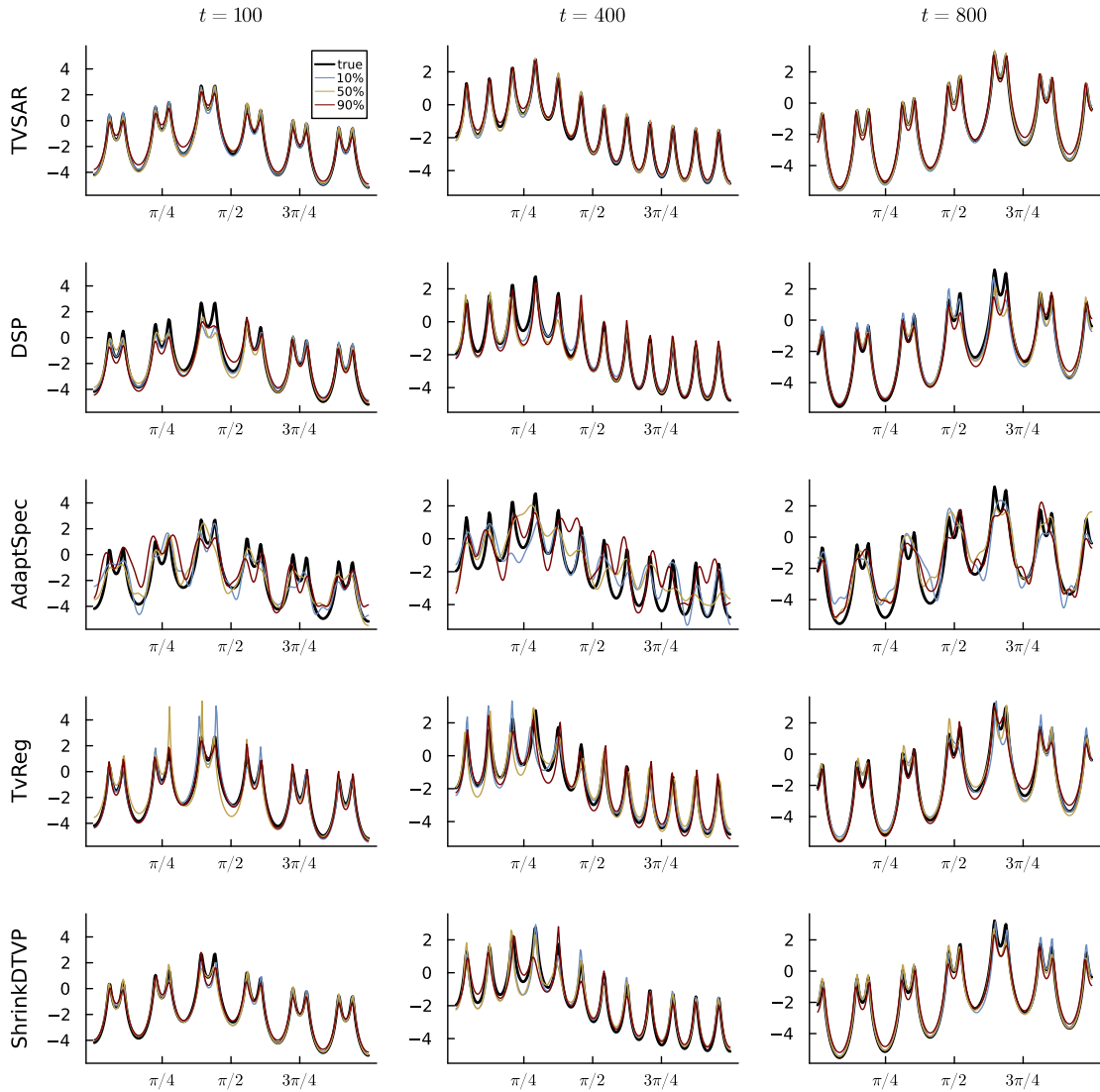


Figure S7: Experiment 1. Log spectral density at three different time points. The black line is the true spectral density and the three colored lines are the posterior medians from three different datasets chosen from the MSE percentiles.

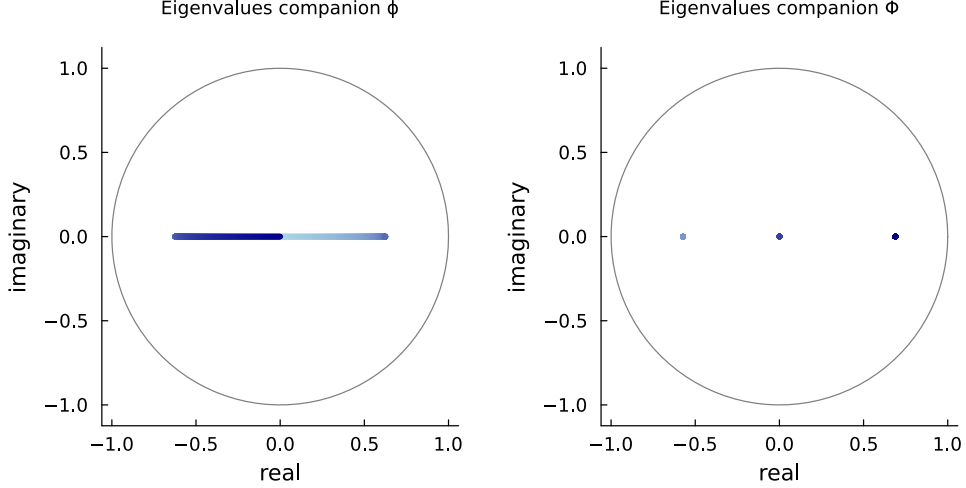


Figure S8: SAR(1,1). Eigenvalues for the companion matrix of the regular and seasonal polynomials over time for the data generating process. The color scale for the eigenvalues represents time, with darker colors indicating later time points.

### S5.3 Experiment 2

The second experiment simulates data from a multi-seasonal TVSAR with two seasonal periods  $\mathbf{s} = (4, 12)$ , non-seasonal order  $p = 1$  and seasonal orders  $\mathbf{P} = (1, 1)$  (i.e., one lag for each seasonal period). This corresponds to the TVSAR( $p = 1, \mathbf{P} = [1, 1]$ )<sub>[4,12]</sub> model

$$(1 - \phi_{11t}L)(1 - \Phi_{11t}L^4)(1 - \Phi_{21t}L^{12})y_t = \varepsilon_t, \quad (\text{S5.6})$$

with  $\varepsilon_t \sim N(0, 1)$ . The time evolution of the unrestricted non-seasonal parameter is given by

$$\theta_{11t} = 0.8 \sin(2\pi t/T) \text{ for } t = 1, \dots, 1000, \quad (\text{S5.7})$$

while the unrestricted parameters in the two seasonal periods follow

$$\Theta_{21t} = 0.5 \text{ for all } t \quad \Theta_{31t} = \begin{cases} -0.50 & \text{for } t = 1, \dots, 250 \\ 0 & \text{for } t = 251, \dots, 750 \\ 0.95 & \text{for } t = 751, \dots, 1000. \end{cases} \quad (\text{S5.8})$$

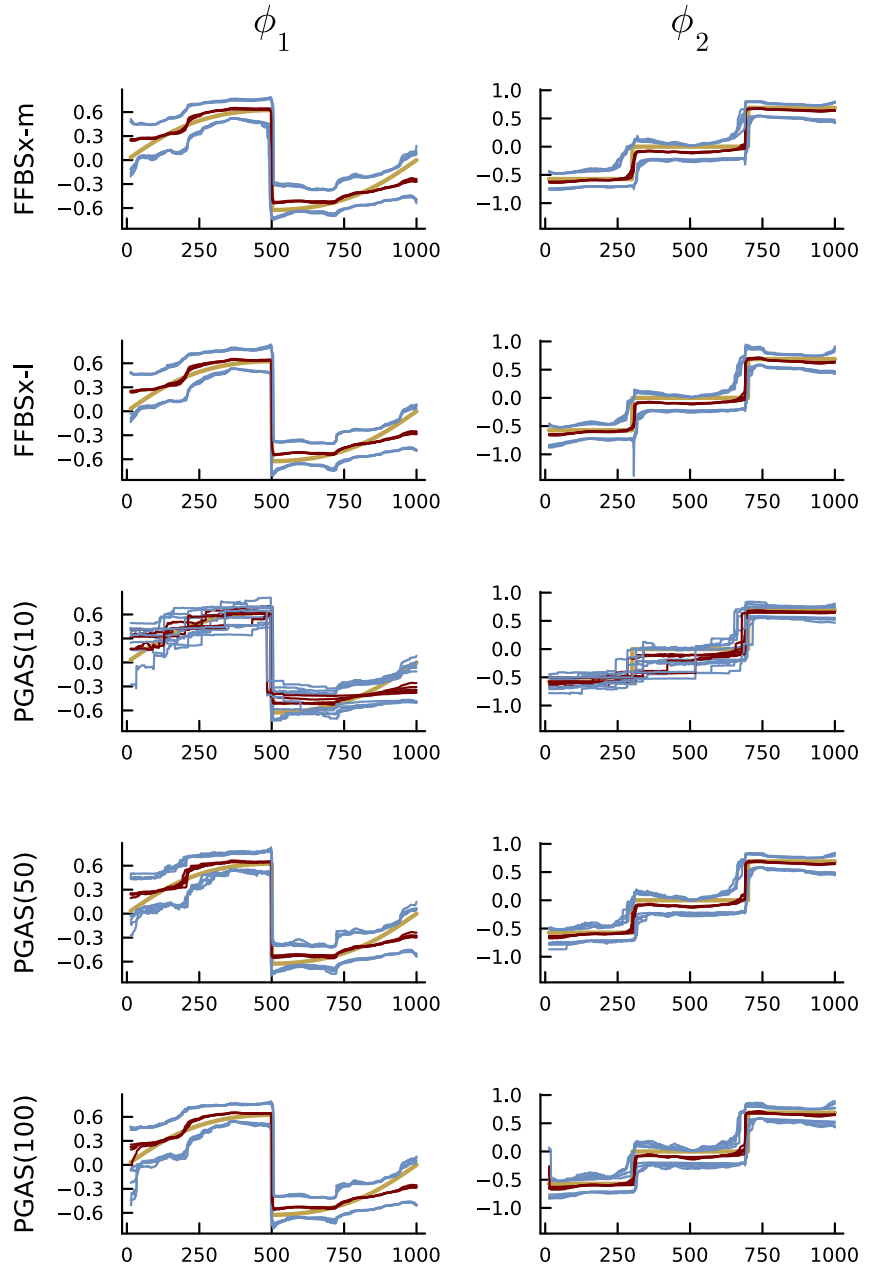


Figure S9: SAR(1,1). Experiment 1. Assessing MCMC convergence by re-estimating the model on the same dataset with five different initial values. The red and blue lines are posterior medians and 95% equal tail credible bands over time for each of the five runs. The beige line is the true parameter evolution in the  $\phi$ -parameterization.

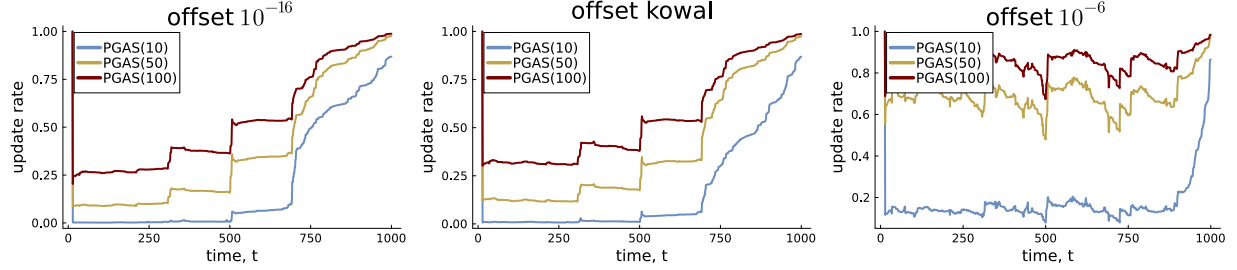


Figure S10: SAR(1,1). PGAS update rates for three offsets in the log-volatility model for  $\mathbf{h}_t$  for different numbers of particles.

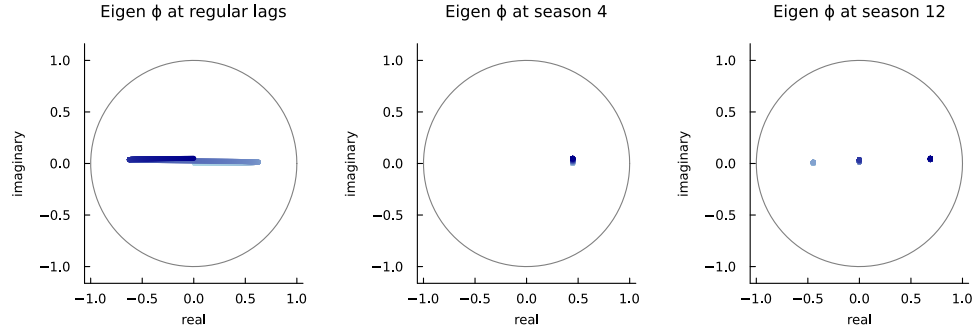


Figure S11: Experiment 2. Eigenvalues for the companion matrix of the regular and seasonal polynomials over time for the data generating process. The color scale for the eigenvalues represents time, with darker colors indicating later time points.

Figure S11 shows the time evolution of the eigenvalues of the companion matrix of the regular and seasonal AR coefficients; the eigenvalues are slightly jittered to avoid complete overlap. Table S3 displays effective sample sizes for spectral density estimates for the different posterior algorithms for the TVSAR model. Figure S12 explores the convergence of estimates from different algorithm over five different initial values; similarly to Experiment 1, the FFBSx posteriors are similar from different initial values, and PGAS needs up to 100 particles to give stable results. Figures S13-S16 give additional results for Experiment 2.

## S5.4 Experiment 3 - Redundant lags

Experiments 1 and 2 use the correct number of regular and seasonal lags. The empirical application in Section 5 uses the log predictive scores to determine the optimal number of lags. This third and final experiment shows that the dynamic shrinkage prior is able to

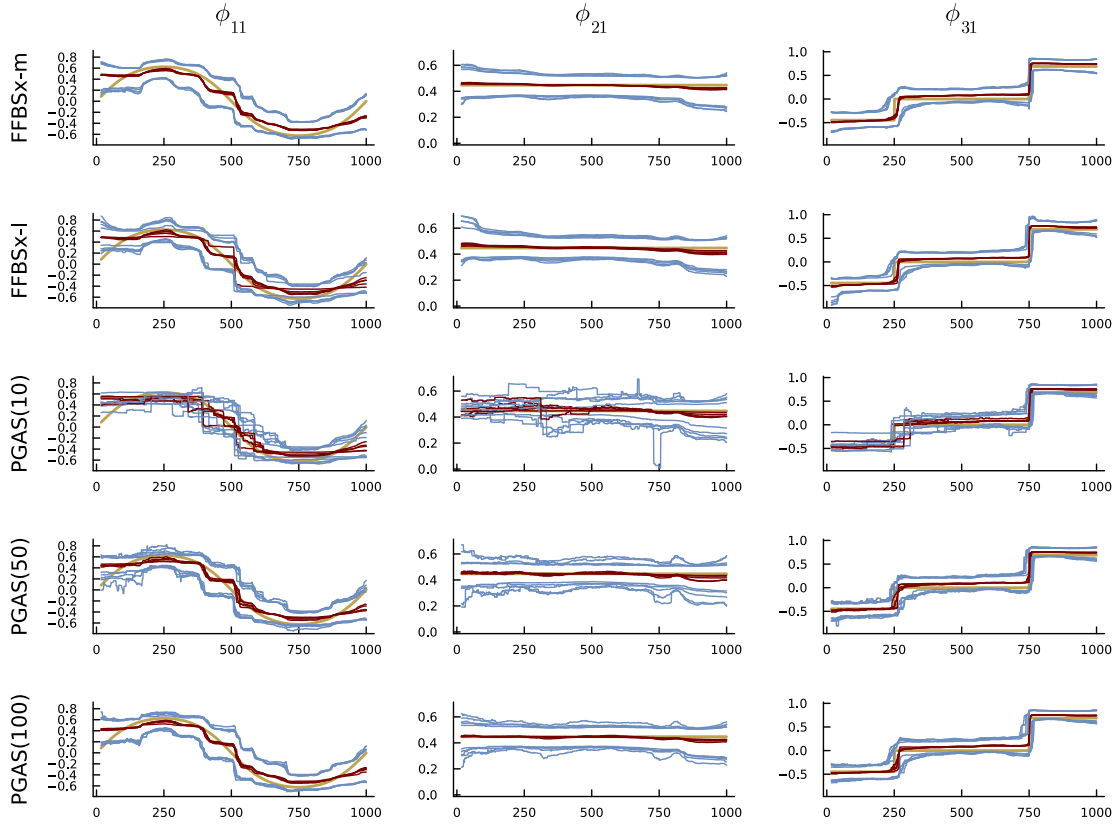


Figure S12: Experiment 2. Assessing MCMC convergence by re-estimating the model on the same dataset with five different initial values. The red and blue lines are posterior medians and 95% equal tail credible bands over time for each of the five repeated runs. The beige line is the true parameter evolution in the  $\phi$ -parameterization.

FFBSx-m			FFBSx-l			PGAS(100)					
	$\pi/4$	$\pi/2$	$3\pi/4$		$\pi/4$	$\pi/2$	$3\pi/4$		$\pi/4$	$\pi/2$	$3\pi/4$
$t = 100$	498	514	482		593	606	587		226	237	215
$t = 400$	368	542	337		411	563	375		257	333	238
$t = 800$	483	597	505		496	767	536		412	620	457

Table S3: Experiment 2. Effective sample size (ESS) for estimating the spectral density for three algorithms. ESS for the spectral density is computed at three selected time points (rows) and at three selected frequencies (columns). The ESS is from an initial posterior sample of 10 000 draws thinned down to 1000 draws. An offset of  $10^{-16}$  is used.

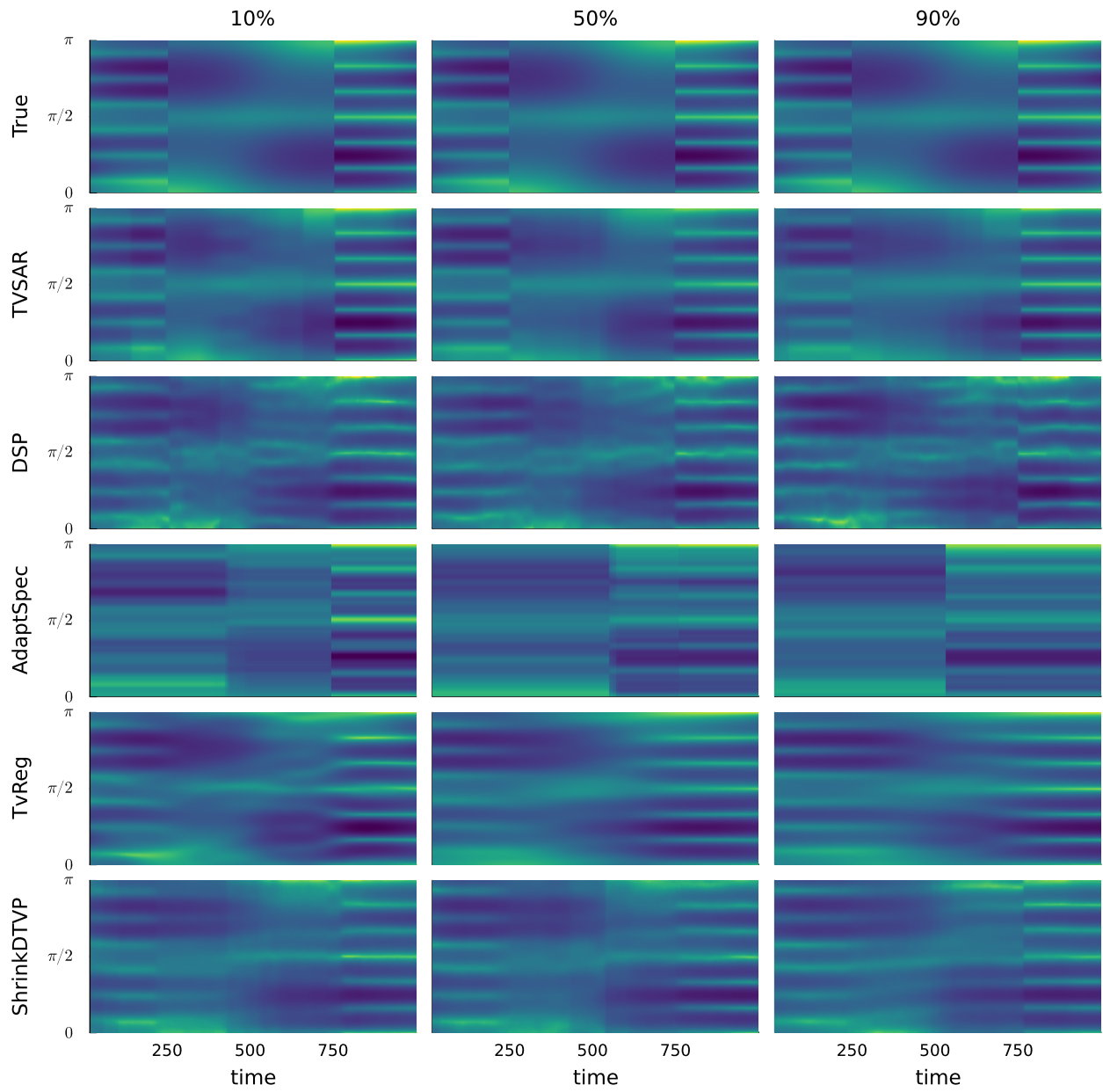


Figure S13: Experiment 2. Heat maps of the estimated spectrogram for the different methods. The columns correspond to different datasets chosen from the percentiles of each model's MSE distribution, to show the performance of each model when it performs well (10%), average (50%) and poorly (90%).

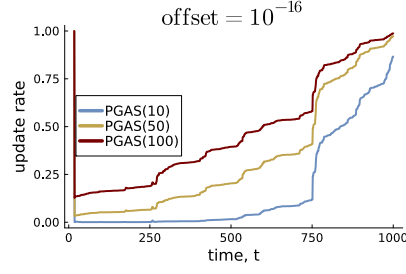


Figure S14: Experiment 2. PGAS update rates for draws using the smallest offset  $10^{-16}$  in the log-volatility model for  $\mathbf{h}_t$  for different numbers of particles.

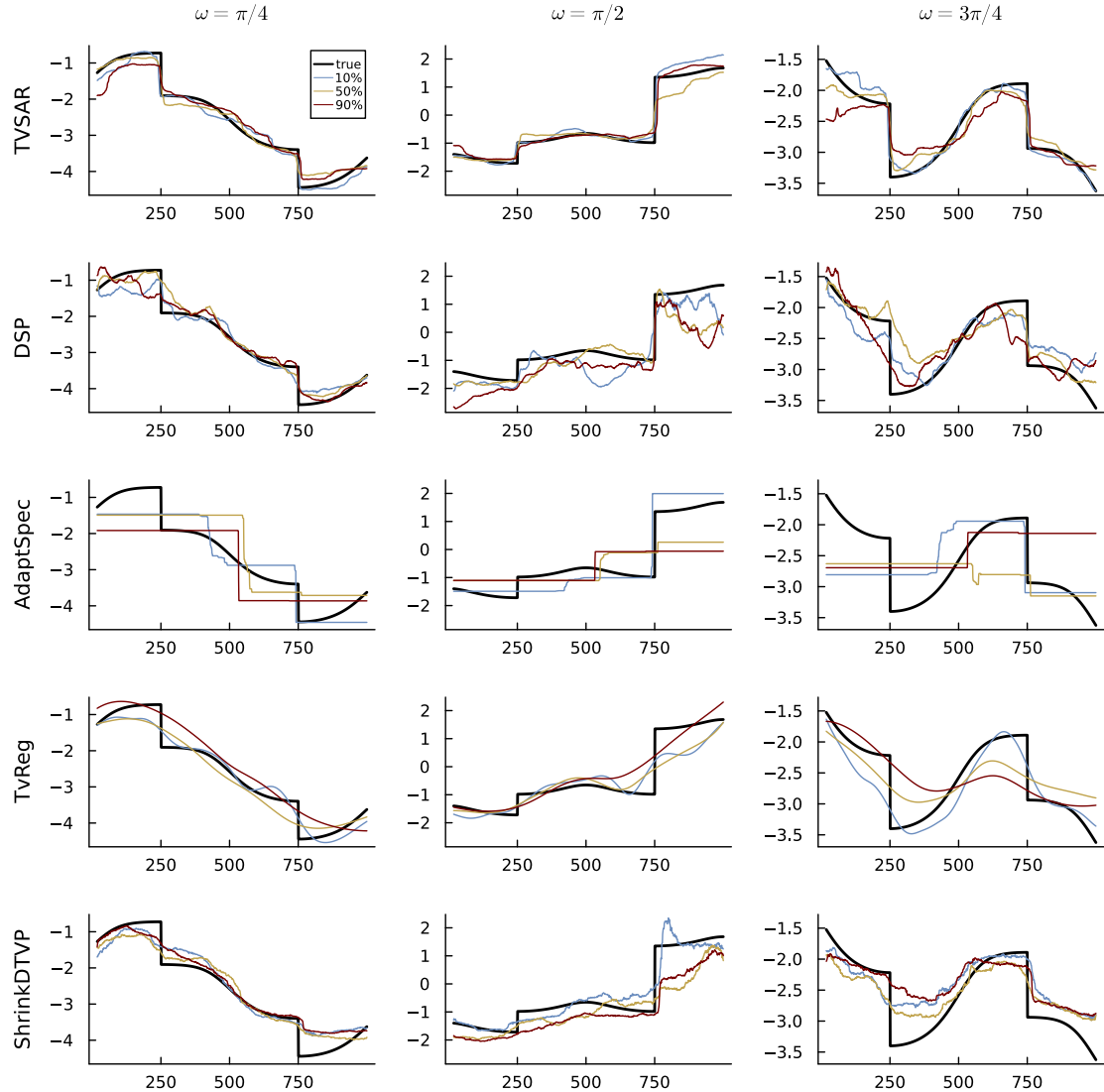


Figure S15: Experiment 2. Time evolution of the log spectral density at three frequencies. The black line is the true spectral density and the three colored lines are the posterior median from three different datasets chosen from the MSE percentiles.

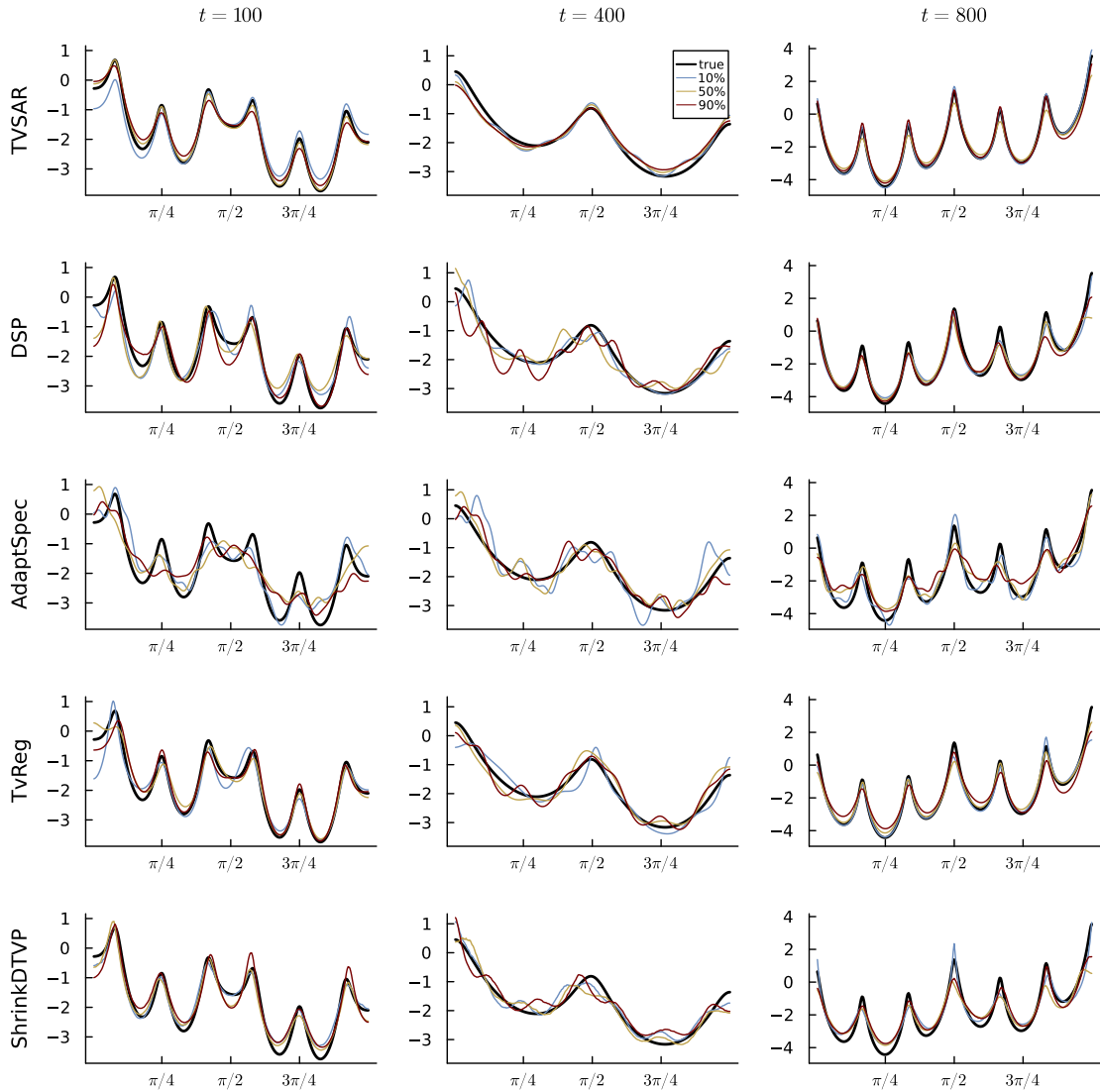


Figure S16: Experiment 2. Log spectral density at three time points. The black line is the true spectral density and the three colored lines are the posterior median from three different datasets chosen from the MSE percentiles.

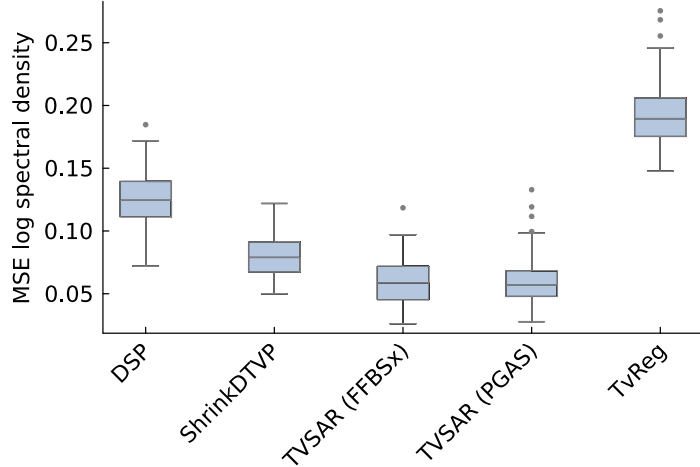


Figure S17: Experiment 3. Box plots of the MSE for the log spectral density over time and frequency from 100 simulated datasets.

effectively shrink redundant lags to zero in the TSVAR model when it has redundant lags. We simulate data from the model in Experiment 1, but with the coefficients for the second regular and second seasonal lags set to zero for all  $t$ . We then fit misspecified models with two regular and two seasonal lags.

Figure S17 shows that fitting a  $\text{TVSAR}(2, 2)_{12}$  to data from a  $\text{TVSAR}(1, 1)_{12}$  still performs well, i.e. the TSVAR model is able to shrink the time trajectory of redundant lags to zero for all  $t$ ; see Figure S18.  $\text{TvReg}$ , which is the only time-domain model without shrinkage, clearly suffers from the redundant parameters and is substantially worse than  $\text{ShrinkDTVP}$  here. Figures S19-S21 give additional results for Experiment 3.

To further demonstrate that the model can effectively shrink redundant lags to zero, we conduct additional simulation experiments. Figures S27 - S30 summarize the results of fitting several over-specified models -  $\text{TVSAR}(3, 3)_{12}$ ,  $\text{TVSAR}(4, 4)_{12}$ ,  $\text{TVSAR}(p = 1, \mathbf{P} = [1, 1])_{[4,12]}$ ,  $\text{TVSAR}(p = 1, \mathbf{P} = [2, 2])_{[4,12]}$  and  $\text{TVSAR}(1, 1)_4$  - to data generated from the true  $\text{TVSAR}(1, 1)_{12}$  in Experiment 3. Each experiment was replicated five times to assess the stability of the estimation procedure.

Figures S24 - S26 show that when fitting  $\text{TVSAR}(3, 3)_{12}$  to data from  $\text{TVSAR}(1, 1)_{12}$ , the model consistently identifies the extra lags as irrelevant across the three different datasets

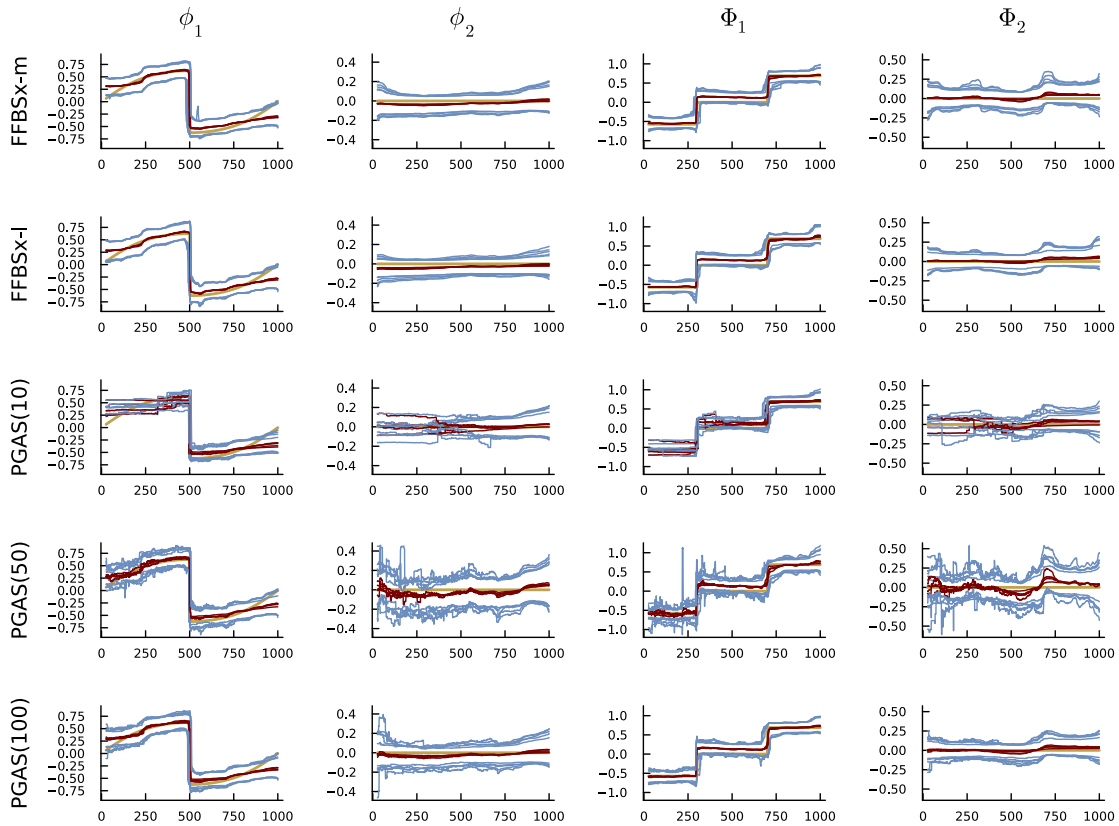


Figure S18: Experiment 3. Assessing MCMC convergence by re-estimating the model using five different initial values drawn from the prior of the global hyperparameters  $\mu$  and  $\kappa$ . All runs are for the same dataset. The red and blue lines are posterior medians and 95% equal tail credible bands over time for each of the five repeated runs. The beige line is the true parameter evolution.

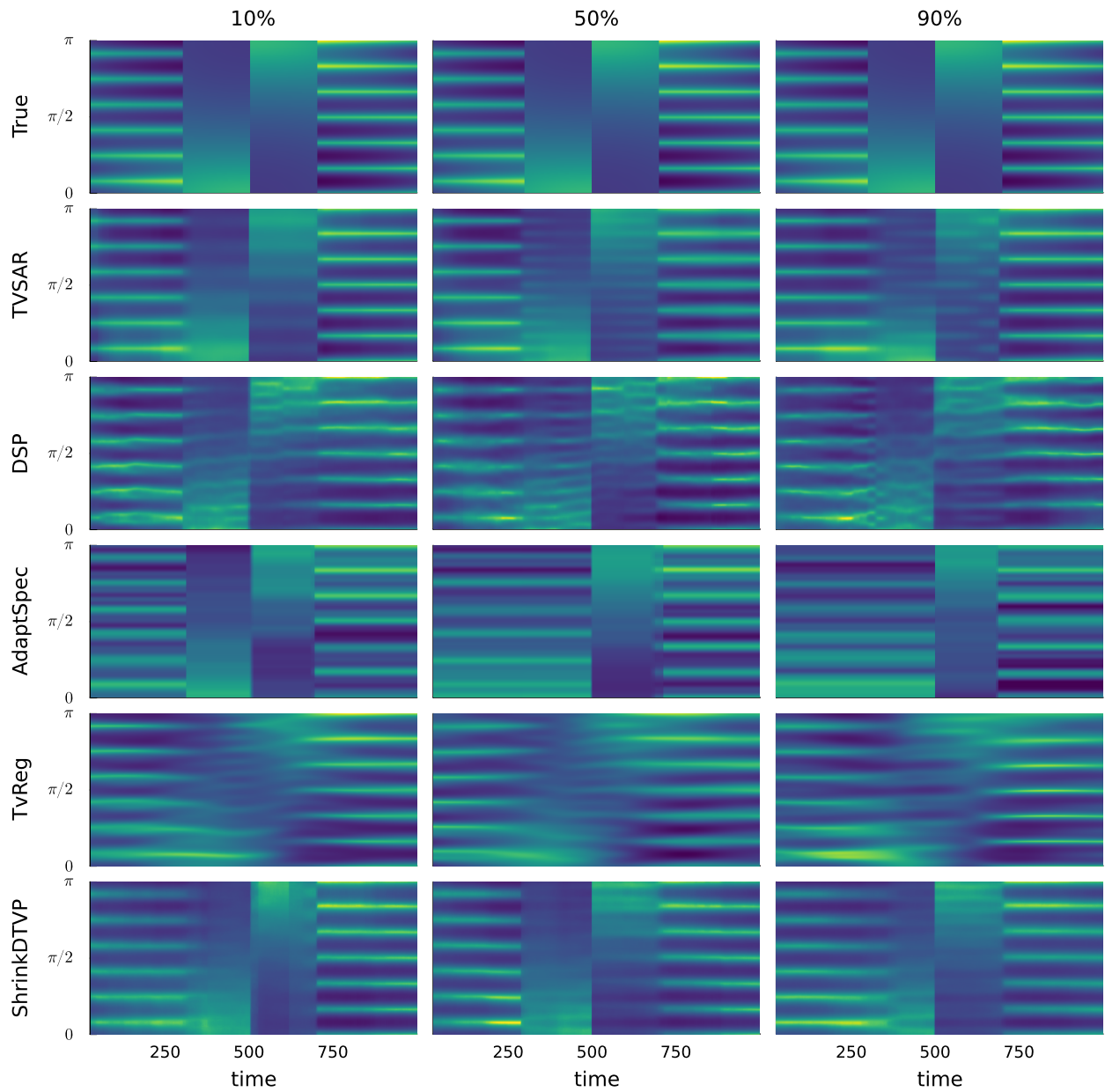


Figure S19: Experiment 3. Heatmaps of the estimated spectrogram for the different methods. The columns correspond to different datasets chosen from the percentiles of each model's MSE distribution, to show the performance of each model when it performs well (10%), average (50%) and poorly (90%).

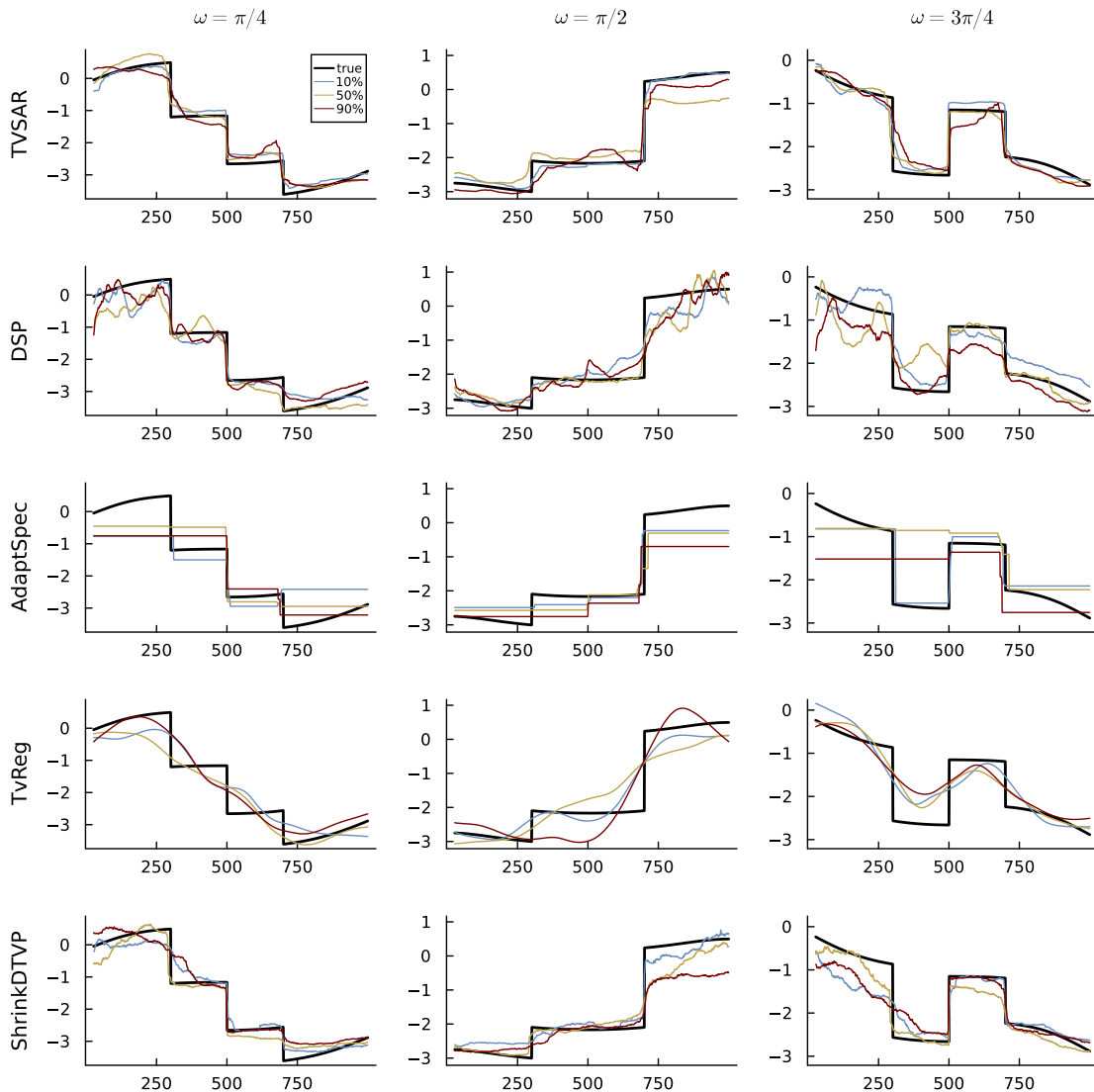


Figure S20: Experiment 3. Time evolution of the log spectral density at three different frequencies. The black line is the true spectral density and the three colored lines are the posterior median from three datasets chosen from the MSE percentiles.

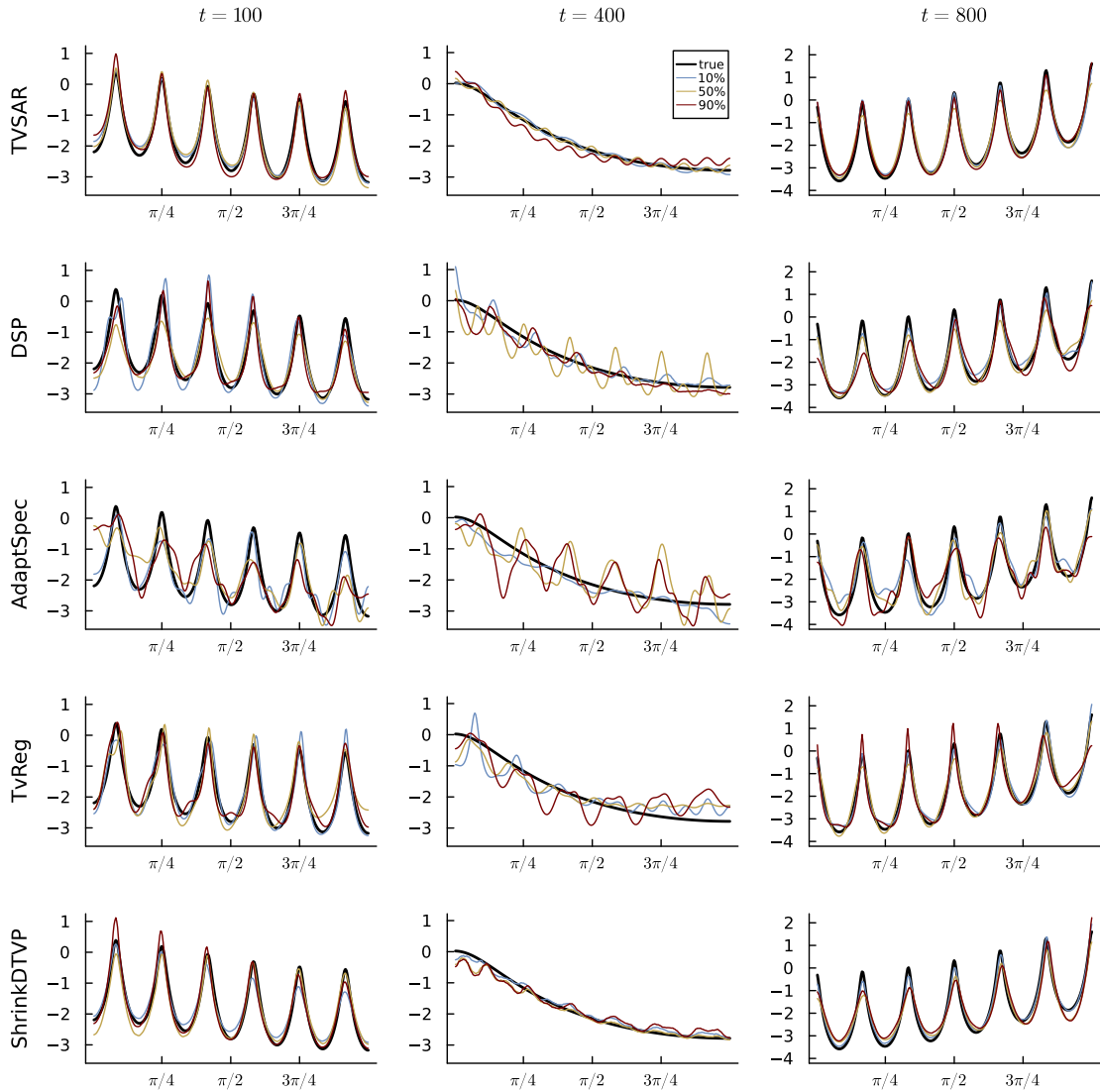


Figure S21: Experiment 3. Log spectral density at three different time points. The black line is the true spectral density and the three colored lines are the posterior median from three datasets chosen from the MSE percentiles.

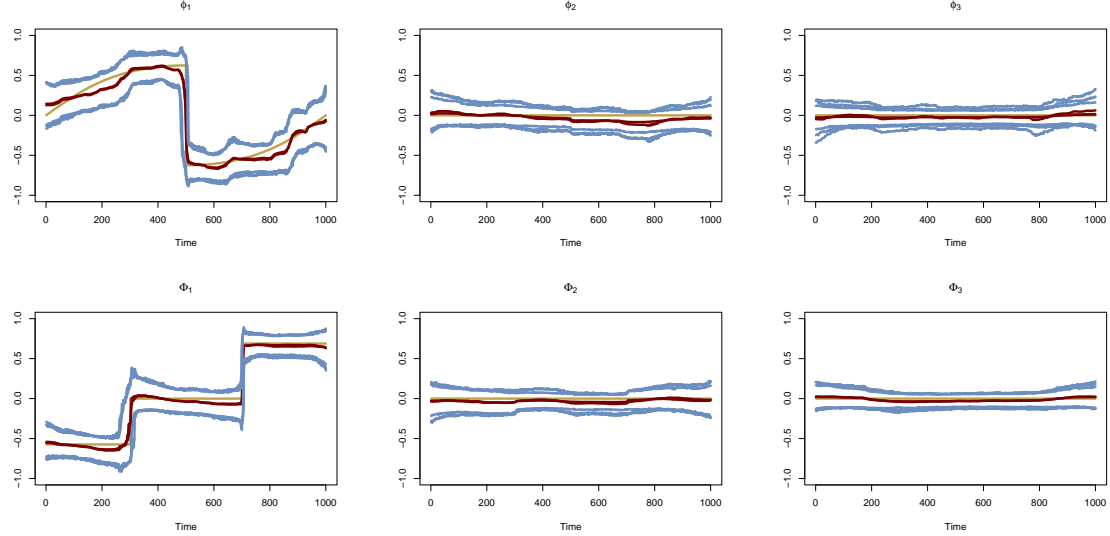


Figure S22: Fitting TVSAR(3,3)<sub>12</sub> model to data generated from a TVSAR(1,1)<sub>12</sub>. MCMC convergence is assessed by re-estimating the model using three different seeds for the same dataset. The red and blue lines are posterior medians and 95% HDIs over time for each of the three repeated runs. The beige line is the true parameter evolution.

considered.

Figure S27 provides a closer look at fitting TVSAR(4,4) for a single dataset. Here the model correctly shrinks three redundant lags to zero; however, when the number of unnecessary lags increases, the MCMC sampler exhibits slower convergence, indicating some loss of stability, particularly at the fourth lag.

Figures S29 - S30 illustrate fits of models with extra seasonal lags with period four, TVSAR( $p = 1, \mathbf{P} = [1, 1]$ )<sub>[4,12]</sub> and TVSAR( $p = 1, \mathbf{P} = [2, 2]$ )<sub>[4,12]</sub>, respectively. In both cases, the posteriors successfully drive the redundant coefficients to zero.

Finally, Figure S30 demonstrates a seasonally misspecified fit, where TVSAR(1,1)<sub>4</sub> is applied to data from TVSAR(1,1)<sub>12</sub>.

Overall, the model performs well in detecting and shrinking redundant lags but shows some limitations when the degree of over-specification becomes large. Poor mixing of the dynamic shrinkage priors may contribute to this behavior.

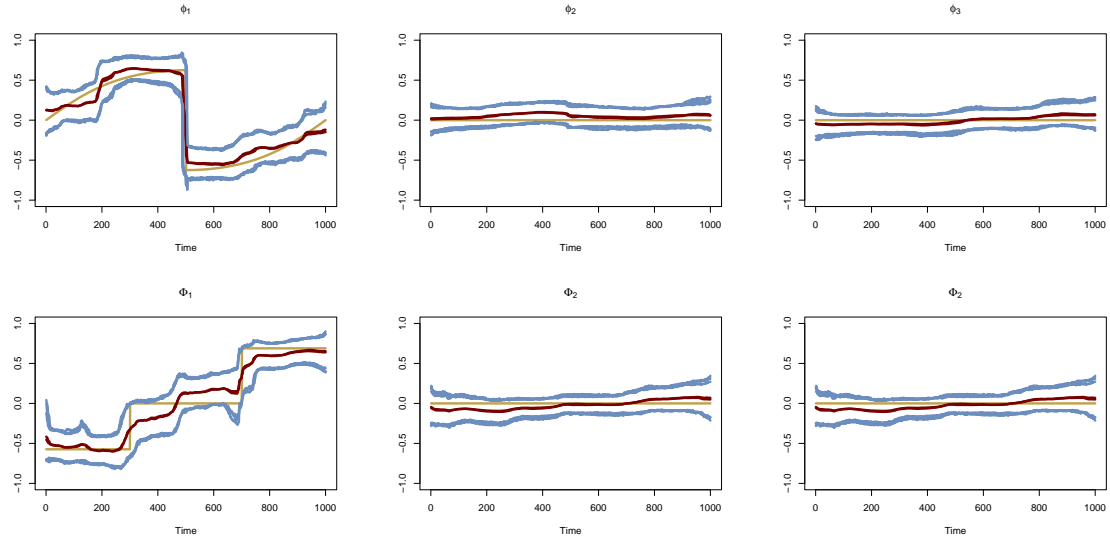


Figure S23: Fitting TVSAR(3,3)<sub>12</sub> model to data generated from a TVSAR(1,1)<sub>12</sub>. MCMC convergence is assessed by re-estimating the model using three different seeds for the same dataset. The red and blue lines are posterior medians and 95% HDIs over time for each of the three repeated runs. The beige line is the true parameter evolution.

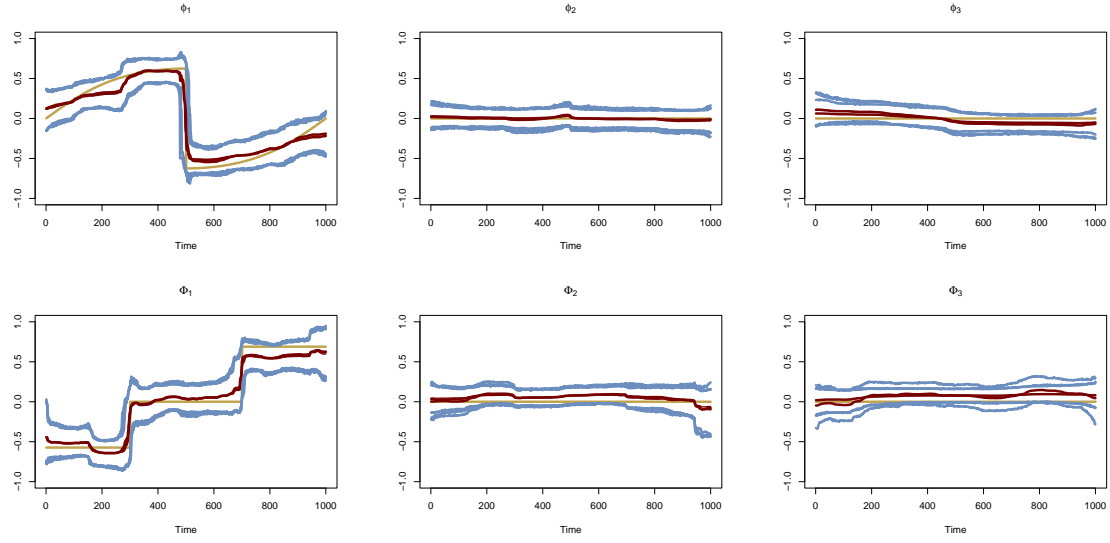


Figure S24: Fitting TVSAR(3,3)<sub>12</sub> model to data generated from a TVSAR(1,1)<sub>12</sub>. MCMC convergence is assessed by re-estimating the model using three different seeds for the same dataset. The red and blue lines are posterior medians and 95% HDIs over time for each of the three repeated runs. The beige line is the true parameter evolution.

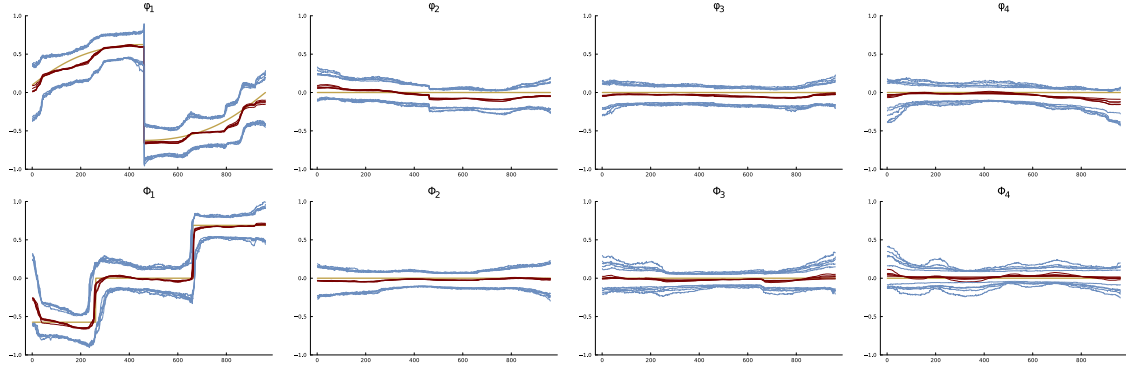


Figure S25: Fitting TVSAR(4, 4)<sub>12</sub> model to data generated from a TVSAR(1, 1)<sub>12</sub>. MCMC convergence is assessed by re-estimating the model using three different seeds for the same dataset. The red and blue lines are posterior medians and 95% HDIs over time for each of the three repeated runs. The beige line is the true parameter evolution.

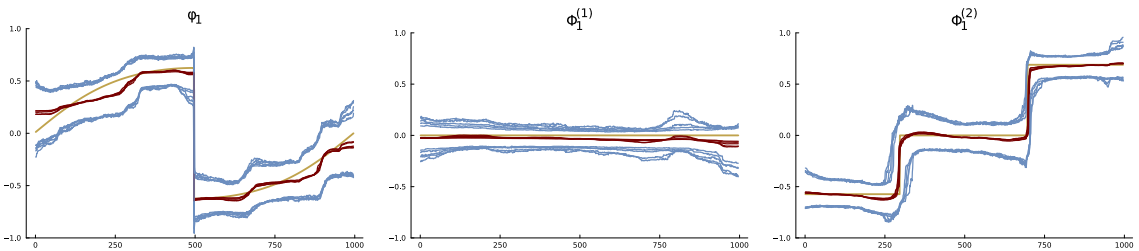


Figure S26: Fitting TVSAR( $p = 1, P = [1, 1]$ )<sub>4,12</sub> model to data generated from a TVSAR(1, 1)<sub>12</sub>. MCMC convergence is assessed by re-estimating the model using three different seeds for the same dataset. The red and blue lines are posterior medians and 95% HDIs over time for each of the three repeated runs. The beige line is the true parameter evolution.

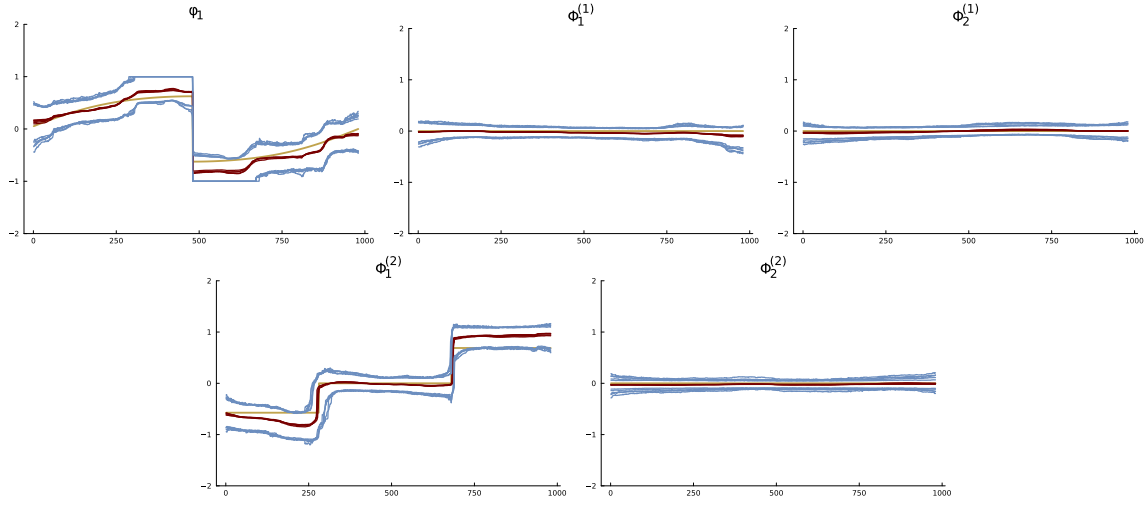


Figure S27: Fitting  $\text{TVSAR}(p = 1, P = [2, 2])_{4,12}$  model to data generated from a  $\text{TVSAR}(1, 1)_{12}$ . MCMC convergence is assessed by re-estimating the model using three different seeds for the same dataset. The red and blue lines are posterior medians and 95% HDIs over time for each of the three repeated runs. The beige line is the true parameter evolution.

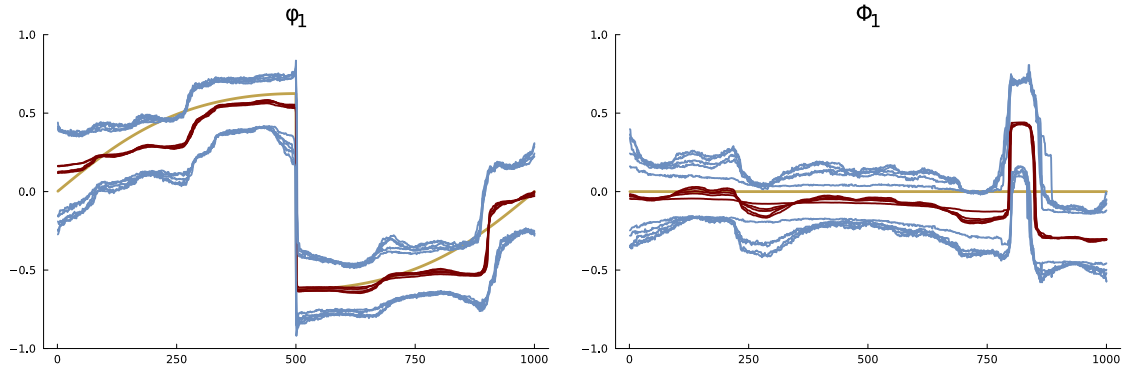


Figure S28: Fitting  $\text{TVSAR}(1, 1)_4$  model to data generated from a  $\text{TVSAR}(1, 1)_{12}$ . MCMC convergence is assessed by re-estimating the model using three different seeds for the same dataset. The red and blue lines are posterior medians and 95% HDIs over time for each of the three repeated runs. The beige line is the true parameter evolution.

## S6 Additional results - US industrial production

Figure S29 assesses the convergence of the FFBS-x algorithm on the US industrial production data by plotting the posterior medians and equal-tail 95% credible intervals from three runs, each with different initial values. The initial values for the global parameters are set so that  $\mu_k = \mu$  and  $\kappa_k = \kappa$  for all  $k$ , with  $\mu$  and  $\kappa$  drawn from their respective priors in each run of the algorithm.

Figure S30 plots the posterior median and equal-tail 95% credible bands from the PGAS algorithm with 100 particles for the US industrial production data.

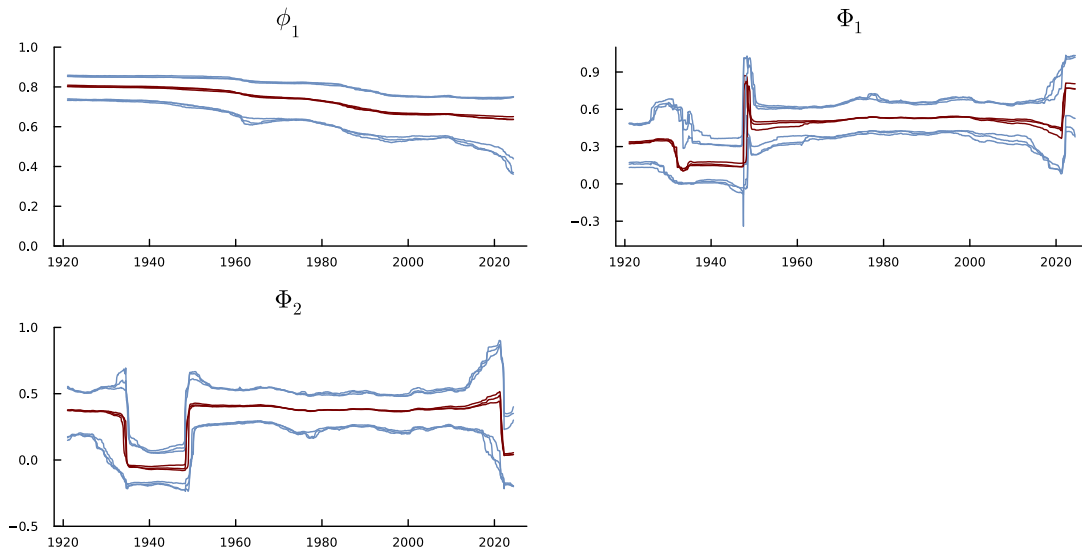


Figure S29: US industrial production. The posterior median and 95% credible intervals from the SAR(1,2) model with dynamic shrinkage prior and stochastic volatility, obtained with the FFBSx algorithm using an offset of  $10^{-16}$ . The posterior median and 95% credible intervals are shown for three runs based on different initial values drawn from the prior.

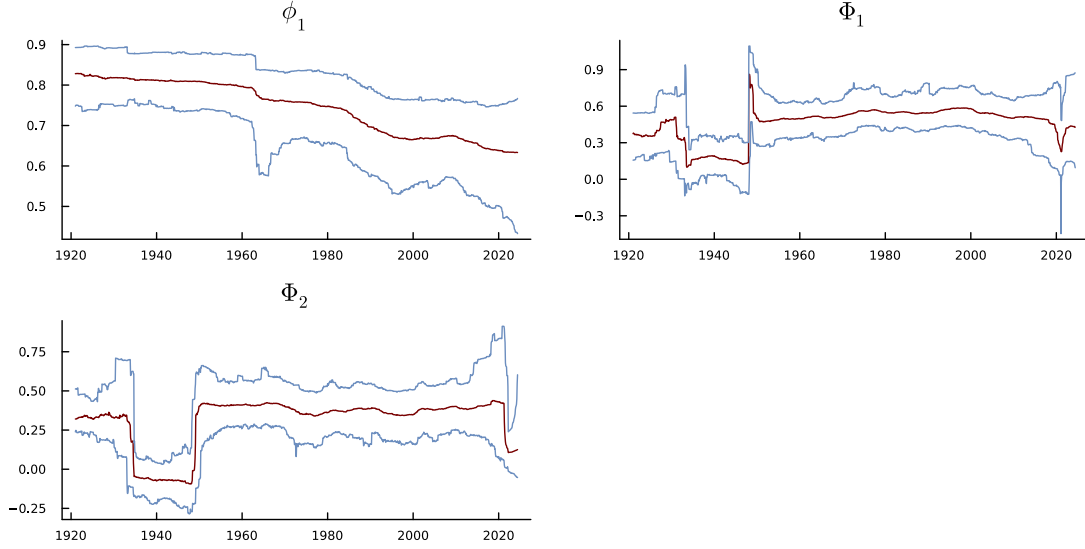


Figure S30: US industrial production. Posterior from SAR(1,2) model with stochastic volatility obtained with the PGAS algorithm with  $N = 100$  particles using an offset of  $10^{-16}$ .

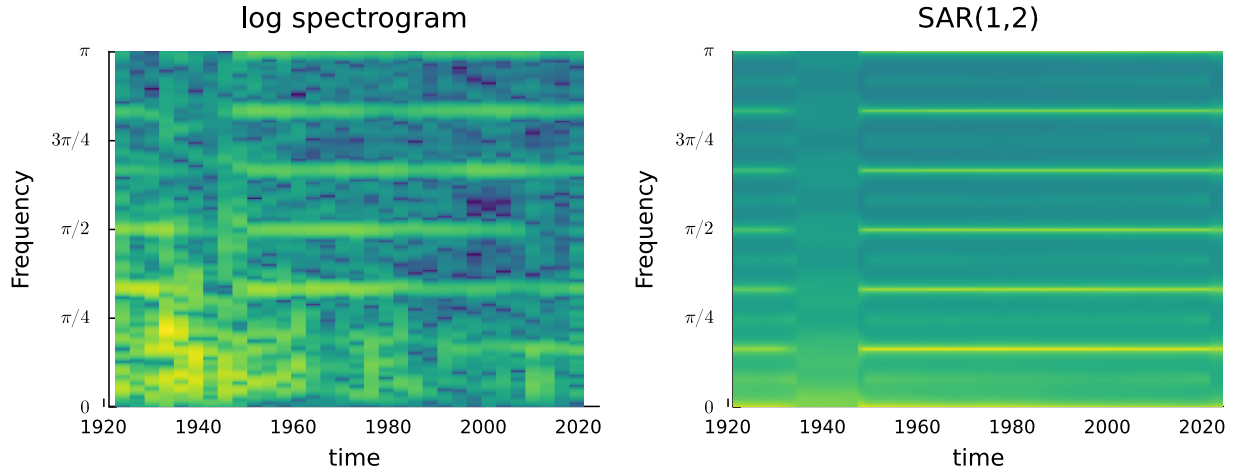


Figure S31: US industrial production. Left: Nonparametric log spectral density over time estimated by Hanning tapered periodograms over overlapping sliding windows of 120 months, moving 36 months between each window; note that 18 months (half the window width) are lost in the beginning and at the end of the time period. Right: posterior median time varying log spectral density from the TVSAR(1,2) model.

Table S4 presents the computing time of the FFBsX sampler for subsets of different lengths of the industrial production time series, and for different dimensions of the state. Both the DSP sampler (Kowal et al., 2019) and the Kalman-based sampling of the state (Thrun

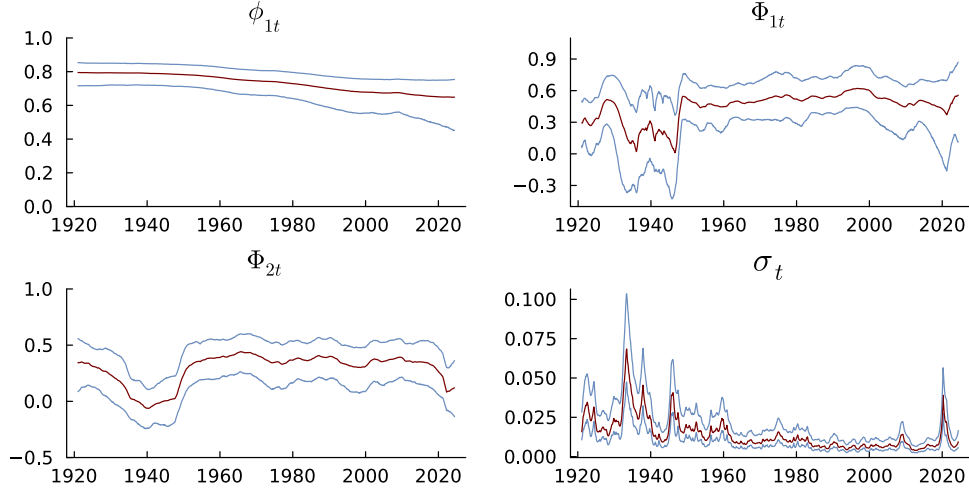


Figure S32: US industrial production. Posterior from FFBSx in the  $\text{TVSAR}(1,2)_{12}$  model with homoscedastic Gaussian parameter innovations and stochastic volatility.

et al., 2005) are known to scale linearly in the length of the time series. The computations were performed with unoptimized Julia code where the computing time can be reduced substantially by removing type instabilities and allocating less memory.

Table S4: Computational times in seconds for 1,000 posterior draws using the FFBSx sampler applied to subsets of different lengths of the industrial production time series.

	SAR(1,1)	SAR(2,2)	SAR(3,3)	SAR(4,4)	SAR(5,5)
N of state variables	13	26	39	52	65
$T = 300$	5	7	11	13	16
$T = 600$	9	13	18	29	42
$T = 1200$	18	24	35	45	63

## S7 Computing the log predictive scores

The LPS in Table 1 are based on three separate Gibbs sampling runs. The LPS estimates are computed by running a Gibbs sampler to obtain 10 000 posterior parameter draws after a burn-in sample of 3000 draws for each the 120 observations in the test set. Using these draws, the predictive density at the test data point  $y_t$  is estimated by the Monte Carlo average

$$p(y_t|y_{1:(t-1)}) = \iint p(y_t|\mathbf{x}_t, \boldsymbol{\theta}_t, \sigma_t) p(\boldsymbol{\theta}_t, \sigma_t|y_{1:(t-1)}) d\boldsymbol{\theta}_t d\sigma_t \approx J^{-1} \sum_{j=1}^J p(y_t|\mathbf{x}_t, \boldsymbol{\theta}_t^{(j)}, \sigma_t^{(j)}), \quad (\text{S7.1})$$

where  $\boldsymbol{\theta}_t^{(j)}$  and  $\sigma_t^{(j)}$  uses draws from the joint posterior  $p(\boldsymbol{\theta}_{0:(t-1)}, \mathbf{h}_{0:(t-1)}, \sigma_{1:(t-1)}, \boldsymbol{\mu}, \boldsymbol{\kappa}|y_{1:(t-1)})$  and the model's parameter evolution to draw  $\boldsymbol{\theta}_t$ ,  $\mathbf{h}_t$  and  $\sigma_t$ . The LPS estimate is then obtained by summing the log predictive density evaluations over the test periods

$$\text{LPS} = \sum_{t=t^*}^T \text{LPS}_t, \quad (\text{S7.2})$$

where  $\text{LPS}_t = \log p(y_t|y_{1:(t-1)})$  and  $t^*$  is the first time point in the test dataset.

A reviewer pointed out that the estimate in (S7.1) can be made more precise in conditionally linear Gaussian state-space models by using the Kalman filter to analytically integrate out the state trajectory (see Section A.1.2 in the supplementary material to Bitto and Frühwirth-Schnatter (2019)). A similar estimator is possible here by analytically integrating out the state using the extended Kalman filter; this will rely on the Gaussian approximation underlying the FFBSx algorithm also in the LPS computation, but the additional bias may be worthwhile from the reduction in variance. A bigger challenge with both approaches, however, is that the computational cost of LPS is substantial, unless a cluster is available to estimate the  $\text{LPS}_t$  for  $t = t^*, \dots, T$  across the compared models in parallel. A more practical approach is to use an information criteria to choose the number of lags over local segments of the time series, and then fit the TVSAR with the maximal number of regular

and seasonal lags over the segments. As shown in Experiment 3, the potential redundant lags will be shrunk to zero by the dynamic shrinkage process prior. We proceed with the TVSAR(1, 2)<sub>12</sub> model in this section, but model comparison and evaluation for the TVSAR model and other state-space models with global-local shrinkage processes are important topics for future research.

## S8 Performance near the non-stable region

As discussed in Section 6, the FFBSx sampler for the TVSAR model with stability restrictions can generate a posterior distribution for the parameter evolution that deviates from the true posterior when the data generating process has long spells near the instability region. To illustrate this, we simulate a time series of length  $T = 500$  from a  $\text{TVSAR}(1, 1)_{12}$  where the seasonal polynomial is consistently close to the instability region and the regular AR polynomial is close to the non-stability instability region during certain time periods. A simple Gaussian homoscedastic parameter evolution is used to ensure that the sample from PGAS with 100 particles accurately represents” the true posterior distribution. We fixed the static parameters to their values in the data generating process to clearly isolate the state estimation problem.

The top panel of Figure S33 shows the results when the fitted model has parameters that are *not* restricted to the stability region, while the plots in the bottom panel are for the case with stability restrictions. The true parameter evolution (black line) for the two parameters and the inferred posterior distribution for the fitted  $\text{TVSAR}(1, 1)_{12}$  model are shown for several algorithms. The posterior from PGAS with 100 particles (which was verified to be a good representation of the true posterior distribution since more particles gave very similar results) is shown as a gray line for the posterior median and the gray shaded regions for the 95% credibility intervals. The posteriors from two approximate samplers are also shown: FFBSx based on the extended Kalman filter (denoted by EKF in the graphs) and FFBS based on the unscented Kalman filter (UKF, Julier and Uhlmann (2004)); the unscented Kalman filter uses so-called sigma points instead of linearization and can under some circumstances be seen as a second-order approximation method.

Figure S33 (top panel) shows that when fitting models without imposing stability restrictions, all three sampler give essentially identical results, but the posterior distribution contains substantial probability mass on the non-stable processes. Note that this model is still nonlinear due to the multiplicative seasonal model. The bottom panel of Figure S33 illustrates

the results when the same dataset is fitted with  $\text{TVSAR}(1,1)_{12}$  with stability restrictions imposed. Here the FFBSx sampler gives a distorted posterior compared to the one from PGAS. The FFBS sampler based on the unscented Kalman filter (UKF) improves on the FFBSx. There are several other recently proposed Kalman-based approximate filters in the signal processing literature (Skoglund et al., 2015, 2019; García-Fernández et al., 2015) that can be used in FFBS samplers to more accurately estimate the posterior near the instability region. This is our current focus and will be reported more fully in a separate article. We are also exploring other mappings from the unrestricted parameters to the partial autocorrelations than (2.3), which is used in our article, to improve the performance of the posterior samplers near the instability region.

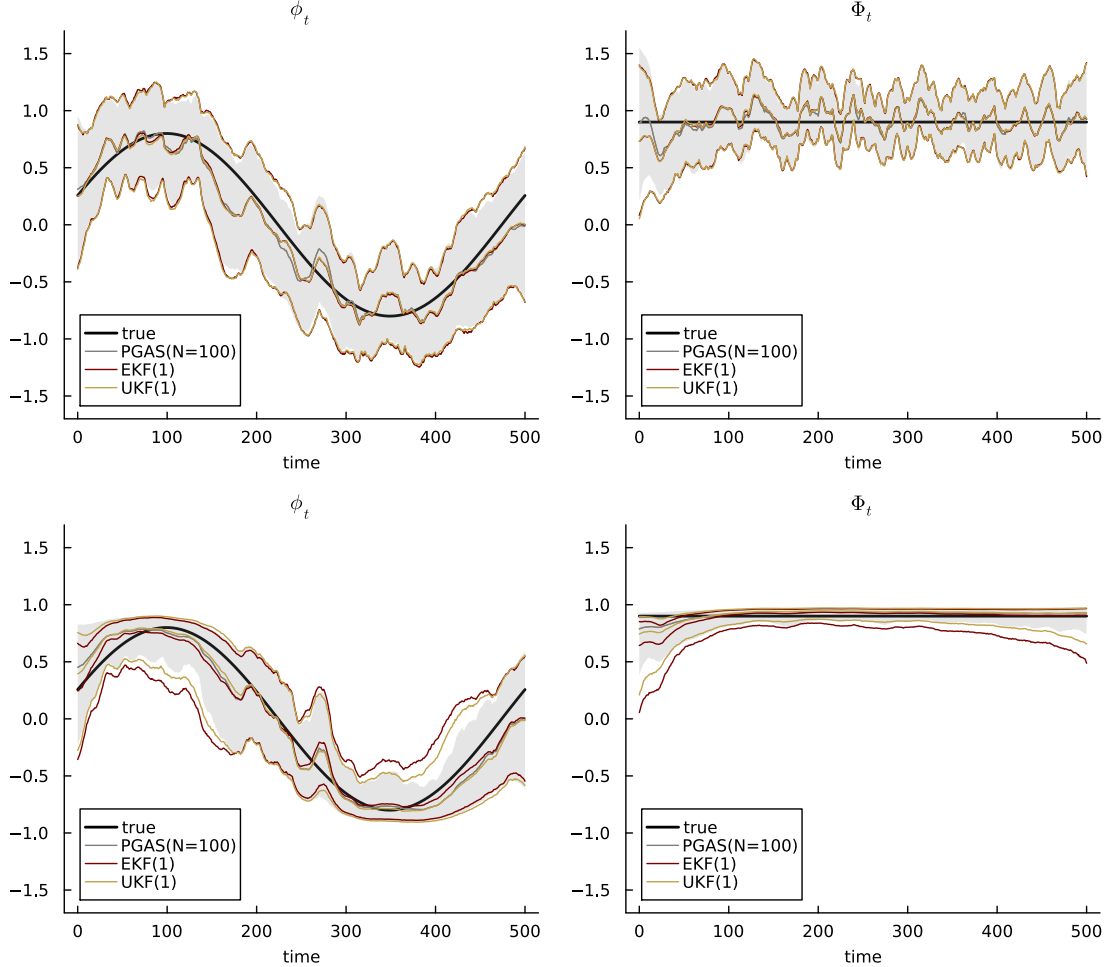


Figure S33: Fitting a  $\text{TVSAR}(1,1)_{12}$  model to a time series from a near non-stable  $\text{TVSAR}(1,1)_{12}$  process. Both the data generating process and the fitted model have homoscedastic Gaussian parameter innovations. In the graphs in the top panel, the parameters are *not* restricted to the stable region. In the bottom panel, the parameters are restricted to the stability region. The gray line and gray shaded regions are the posterior mean and the 95% credible intervals from the PGAS sampler with 100 particles. The posterior from the FFBSx sampler (red lines denoted EKF) and the posterior from FFBS with the unscented Kalman filter (UKF) are also shown.